



HAL
open science

Ophicarbonates evolution from seafloor to subduction and implications for deep-Earth C cycling

E. Cannao, M. Scambelluri, Gray E. Bebout, S. Agostini, T. Pettke,
Marguerite Godard, L. Crispini

► **To cite this version:**

E. Cannao, M. Scambelluri, Gray E. Bebout, S. Agostini, T. Pettke, et al.. Ophicarbonates evolution from seafloor to subduction and implications for deep-Earth C cycling. *Chemical Geology*, 2020, 546, pp.119626. 10.1016/j.chemgeo.2020.119626 . hal-02911651

HAL Id: hal-02911651

<https://hal.umontpellier.fr/hal-02911651v1>

Submitted on 6 Nov 2020

HAL is a multi-disciplinary open access archive for the deposit and dissemination of scientific research documents, whether they are published or not. The documents may come from teaching and research institutions in France or abroad, or from public or private research centers.

L'archive ouverte pluridisciplinaire **HAL**, est destinée au dépôt et à la diffusion de documents scientifiques de niveau recherche, publiés ou non, émanant des établissements d'enseignement et de recherche français ou étrangers, des laboratoires publics ou privés.

1
2
3
4
5
6
7
8
9
10
11
12
13
14
15
16
17
18
19
20
21
22
23
24
25
26
27
28
29
30
31
32
33
34
35
36
37
38
39
40
41
42
43
44
45
46
47
48
49
50
51
52
53
54
55
56
57
58
59
60
61
62
63
64
65

Ophicarbonates evolution from seafloor to subduction and implications for deep-Earth C cycling

E. Cannà^a, M. Scambelluri^b, G. E. Bebout^c, S. Agostini^d, T. Pettke^e, M. Godard^f, L.
Crispini^b

^a *Dipartimento di Scienze della Terra “A. Desio”, Università di Milano, Via Botticelli 23,
21133 Milano, Italy*

^b *Dipartimento di Scienze della Terra, dell’Ambiente e della Vita, Università di Genova, C.so
Europa 26, 16132 Genova, Italy*

^c *Department of Earth and Environmental Sciences, Lehigh University, Bethlehem, PA 18015,
USA*

^d *Istituto di Geoscienze e Georisorse, CNR, Via Moruzzi 1, 56124 Pisa, Italy*

^e *Institute of Geological Sciences, University of Bern, 1+3 Baltzerstrasse, CH-3012, Bern,
Switzerland*

^f *Geosciences Montpellier, CNRS, Université de Montpellier, Place Eugène Bataillon, 34095
Montpellier, France*

1 Abstract

2 The chemical and physical processes operating during subduction-zone metamorphism
3 can profoundly influence the cycling of elements on Earth. Deep-Earth carbon (C) cycling
4 and mobility in subduction zones has been of particular recent interest to the scientific
5 community. Here, we present textural and geochemical data (C-O, Sr isotopes and bulk and
6 *in-situ* trace element concentrations) for a suite of ophicarbonates (carbonate-bearing
7 serpentinites) metamorphosed over a range of peak pressure-temperature (*P-T*) conditions
8 together representing a prograde subduction zone *P-T* path. These rocks, in order of
9 increasing peak *P-T* conditions, are the Internal Liguride ophicarbonates (from the Bracco
10 unit, N. Apennines), pumpellyite- and blueschist-facies ophicarbonates from the Voltri Massif
11 (W. Ligurian Alps) and the Queyras (W. Alps), respectively, and eclogite-facies
12 ophicarbonates from the Voltri Massif. The Bracco oceanic ophicarbonates retain breccia-like
13 textures associated with their seafloor hydrothermal and sedimentary origins. Their trace
14 element concentrations and $\delta^{18}\text{O}_{\text{VSMOW}}$ (+15.6 to +18.2‰), $\delta^{13}\text{C}_{\text{VPDB}}$ (+1.1 to +2.5‰) and
15 their $^{87}\text{Sr}/^{86}\text{Sr}$ (0.7058 to 0.7068), appear to reflect equilibration during Jurassic seawater-rock
16 interactions. Intense shear deformation characterizes the more deeply subducted
17 ophicarbonates, in which prominent calcite recrystallization and carbonation of serpentinite
18 clasts occurred. The isotopic compositions of the pumpellyite-facies ophicarbonates overlap
19 those of their oceanic equivalents whereas the most deformed blueschist-facies sample shows
20 enrichments in radiogenic Sr ($^{87}\text{Sr}/^{86}\text{Sr} = 0.7075$) and depletion in ^{13}C (with $\delta^{13}\text{C}$ as low as -
21 2.0‰). These differing textural and geochemical features for the two suites reflect interaction
22 with fluids in closed and open systems, respectively. The higher-*P*-metamorphosed
23 ophicarbonates show strong shear textures, with coexisting antigorite and dolomite, carbonate
24 veins crosscutting prograde antigorite foliation and, in some cases, relics of magnesite-
25 nodules enclosed in the foliation. These rocks are characterized by lower $\delta^{18}\text{O}$ (+10.3 to
26 13.0‰), enrichment in radiogenic Sr ($^{87}\text{Sr}/^{86}\text{Sr}$ up to 0.7096) and enrichment in incompatible

27 and fluid-mobile element (FME; e.g., As, Sb, Pb). These data seemingly reflect interaction
28 with externally-derived metamorphic fluids and the infiltrating fluids likely were derived
29 from dehydrating serpentinites with hybrid serpentinite-sediment compositions. The
30 interaction between these two lithologies could have occurred prior to or after dehydration of
31 the serpentinites. We suggest that decarbonation and dissolution/precipitation processes
32 operating in ancient subduction zones, and resulting in the mobilization of C, are best traced
33 by a combination of detailed field and petrographic observations, C, O and Sr isotope
34 systematics (i.e., 3D isotopes), and FME inventories. Demonstration of such processes is key
35 to advancing our understanding of the influence of subduction zone metamorphism on the
36 mobilization of C in subducting reservoirs and the efficiency of delivery of this C to depths
37 beneath volcanic arcs and into the deeper mantle.

38

39 *Keywords: oceanic ophicarbonates; high-pressure ophicarbonates; deep Carbon cycle;*
40 *subduction zone; C-O-Sr isotopes*

41

42 **1. Introduction**

43 Ophicarbonates (i.e., carbonated ultramafic rocks) are potentially important carbon (C)
44 reservoirs influencing the long-term C cycle in the solid Earth. Large volumes of
45 ophicarbonate form by peridotite alteration at the seafloor, causing low- to moderate-
46 temperature (T) serpentinization (e.g., Mével, 2003; O’Hanley, 1996) and carbonation by
47 mixed seawater and alkaline hydrothermal fluids (e.g., Lost City hydrothermal fields, Früh-
48 Green et al., 2004; Kelley et al., 2005; Ludwig et al., 2006). Ophicarbonates display
49 brecciated textures consisting of serpentinite clasts enclosed by sets of carbonate veins and/or
50 by a micrite matrix. Such rocks occur in present-day oceans (e.g., the Atlantic; Bonatti, 1976)
51 and their abundance in ophiolitic complexes documents ophicarbonate formation also in
52 ancient oceans (e.g., Früh-Green et al., 1990; Schwarzenbach et al., 2013; Tartarotti et al.,

53 2019; Weissert and Bernoulli, 1984). Ophicarbonates can also form at depth in subduction
1 54 zones via interaction of (meta)serpentinite with carbonic fluids leading to carbonation of rock-
2
3 55 forming silicates and to C sequestration into oceanic slabs and supra-subduction mantle
4
5 56 (Piccoli et al., 2016; Scambelluri et al., 2016). These two processes together affect C storage
6
7 57 and transport from oceans to subduction zones and the transfer of C-O-H fluids into volcanic
8
9 58 arcs (Alt et al., 2013; Collins et al., 2015; Kerrick and Connolly, 1998; Scambelluri et al.,
10
11 59 2016) or in deeper parts of the mantle.
12
13

14
15 60 Experiments and thermodynamic modelling suggest relative immobility of C in
16
17 61 subducting oceanic crustal rocks to very high pressure-temperatures (P - T) conditions unless
18
19 62 the rocks are infiltrated by H₂O-rich fluids (Collins et al., 2015; Kerrick and Connolly, 2001,
20
21 63 1998; Molina and Poli, 2000; Poli et al., 2009). Studies of exposed high- P / T metamorphic
22
23 64 rocks document some C mobilization during subduction either by decarbonation reactions or
24
25 65 by carbonate dissolution in aqueous fluids (Ague and Nicolescu, 2014; Cook-Kollars et al.,
26
27 66 2014; Frezzotti et al., 2011; Malaspina et al., 2009; Piccoli et al., 2016; Sapienza et al., 2009;
28
29 67 Scambelluri et al., 2016); however, the scale of this related C transport has remained unclear
30
31 68 (see the discussion by Epstein et al. 2019). Field and stable isotope studies of high- P and
32
33 69 ultrahigh-pressure (UHP) metamorphic suites indicate that the extent of C mobilization by
34
35 70 these processes is highly dependent upon the degree to which rocks behave as systems open
36
37 71 to infiltration by externally-derived H₂O-rich fluids (Collins et al., 2015; Epstein et al., 2019).
38
39
40
41
42
43
44

45 72 Serpentinite is pivotal in the subduction zone C cycle because, as the result of antigorite
46
47 73 dehydration, it supplies H₂O to adjacent carbonate rocks, thus potentially driving
48
49 74 decarbonation reactions (i.e., destabilization of carbonates) and carbonate dissolution.
50
51 75 Moreover, serpentine is reactive to C-O-H fluids and sequesters CO₂ from fluids via
52
53 76 carbonation of its silicate minerals (Scambelluri et al., 2016). The study of ophicarbonates is
54
55 77 timely, given recent interest in subduction zone C cycling, and can address the mechanisms of
56
57
58
59
60
61
62
63
64
65

78 C-storage and loss within a single, complex rock system and between serpentinite and
79 carbonate-bearing reservoirs.

80 Abundant petrographic and petrologic work available to date deals with present-day and
81 fossil oceanic ophicarbonates (Bonatti, 1976; Clerc et al., 2014; Collins et al., 2015;
82 Cortesogno et al., 1980; Driesner, 1993; Galli and Togliatti, 1965; Lafay et al., 2017; Treves
83 et al., 1995; Weissert and Bernoulli, 1984); however, less attention has been paid to
84 ophicarbonate evolution during subduction-zone metamorphism (Collins et al., 2015; Debret
85 et al., 2018; Driesner, 1993; Scambelluri et al., 2016). We focused on ophicarbonates exposed
86 in Alpine-Apennine ophiolite sequences representing a wide range of peak metamorphic P - T ,
87 from low- T oceanic conditions recorded by Apennine ophicarbonates, to pumpellyite-,
88 blueschist- and eclogite-facies conditions experienced by ophicarbonates from the Ligurian
89 and the Western Alps. In this paper, based on study of high- P metamorphic rocks, we
90 demonstrate that decarbonation and dissolution/precipitation processes operating in ancient
91 subduction zones are best traced by a combination of detailed field and petrographic
92 observations, FME inventories, and C, O, and Sr isotope systematics (i.e., 3D isotopes).

93

94 **2. Geological setting**

95

96 *2.1. Northern Ligurian Apennine ophicarbonates*

97 In the Northern Ligurian Apennine, ophiolites either occur as large olistoliths (in the
98 sedimentary flysch of the External Liguride Units) or form large coherent bodies (in the
99 Internal Liguride Units). In the latter setting, ophicarbonates (**Fig. 1A**) occur at the
100 stratigraphic top of the serpentinitized mantle (e.g., Cortesogno et al., 1980) and are overlain by
101 pillow basalt and oceanic sediments (i.e., radiolarian cherts, limestone and mudstone). In such
102 a cases, the Moho is commonly represented by preserved primary contacts of serpentinite-
103 ophicarbonate with pillow basalt and, locally, with extensional tectonic breccia and deep

104 oceanic sediments (Alt et al., 2018; Decandia et al., 1998; Lagabrielle, 1987). Thus far,
1 105 tectonic (OCI) and sedimentary (OCII) ophiicarbonates have been distinguished based on
2
3 106 textural and petrographic features (e.g., Lemoine et al., 1987). The OCI type is characterized
4
5
6 107 by polyphase brittle-ductile to brittle deformation (Treves and Harper, 1994). These rocks
7
8 108 display early serpentine formation after mantle minerals and in shear extensional veins,
9
10
11 109 followed by infiltration of CO₂-rich fluids to form a sequence of generations of calcite veins
12
13 110 in response to increasing hydrothermal fluid pressure ($P_{\text{fluid}}/P_{\text{lithostatic}} > 1$). The last brittle
14
15 111 deformation led to formation of veins filled by calcite and talc druses (Treves and Harper,
16
17
18 112 1994). The set of tectonic and hydrothermal structures recorded by the OCI is related to the
19
20 113 tectonic exposure of the oceanic mantle at surface levels under progressively lower
21
22
23 114 temperature conditions at extensional core-complexes at slow-spreading ridges. The OCI
24
25 115 samples are thus representative of extensional fault settings (Treves and Harper, 1994) and are
26
27
28 116 comparable with ophiicarbonates beneath the Lost City hydrothermal vent at the Mid-Atlantic
29
30 117 Ridge (e.g., Ludwig et al., 2006). Tectonic-sedimentary reworking of the exposed
31
32
33 118 serpentinized mantle, coupled with calcite precipitation, leads to the formation of OCII
34
35 119 showing angular to sub-angular serpentinite clasts of varying sizes embedded in a micrite
36
37
38 120 sedimentary matrix (Treves and Harper, 1994). Oxidation and carbonation processes
39
40 121 accompany the hydrothermal alteration, allowing formation of hematite and thus conferring
41
42 122 upon these rocks a typical red color during a process thought to have generated the Ligurian
43
44
45 123 ophi carbonate variety known as *Rosso di Levante* (Galli, 1957).

46
47 124

48 49 125 *2.2 Western Alps*

50
51
52 126 The Alpine architecture consists of large tectonic units of continental and oceanic
53
54 127 affinity (e.g., Dal Piaz et al., 2003): the ophi carbonate rocks studied here belong to the
55
56
57 128 oceanic lithosphere exposed at three main localities of the Upper Penninic nappe stack and
58
59 129 recording progressively higher peak metamorphic P - T during subduction (**Fig. 1**). From lower
60
61
62
63
64
65

130 to higher grade, the sampled localities are: the pumpellyite-actinolite facies Sestri-Voltaggio
1 131 Zone (Ligurian Alps), the blueschist-facies Queyras (Ubaye locality; French Alps), and the
2
3 132 eclogite-facies-metamorphosed Voltri Massif (Ligurian Alps).
4
5

6 133

8 134 *2.2.1 Sestri-Voltaggio zone*

10 135 The Sestri-Voltaggio zone consists of several tectonic units and is believed to represent
11
12
13 136 the N-S junction zone between the Alpine chain and the Northern Apennines (Crispini and
14
15 137 Capponi, 2001). The ophicarbonates rocks sampled in this area belong to the Figogna unit,
16
17
18 138 consisting of oceanic lithospheric mantle comparable to that in the Voltri Massif, but which
19
20 139 escaped eclogite facies metamorphism during Alpine subduction. The metamorphic grade of
21
22
23 140 this unit is pumpellyite-actinolite facies, in the stability field of lawsonite (270-320 °C and 0.6
24
25 141 GPa; Leoni et al., 1996). Here ophicarbonates crop out near the village of Pietralavezzara in
26
27
28 142 decametric-sized slices with N-S orientations (PL samples in **Fig. 1C**). Despite the polyphase
29
30 143 deformation that affected the Figogna unit, the original oceanic sequence showing
31
32
33 144 ophicarbonates on top of the ultramafic and gabbroic basement, and below a volcano-
34
35 145 sedimentary cover, can still be recognized (Crispini and Capponi, 2001).
36

37 146

40 147 *2.2.2 Queyras complex*

42 148 The Queyras complex is part of the Piedmont-Ligurian domain, west of the eclogite-
43
44
45 149 facies Monviso ophiolite and near the contact with the Briançonnais domain (**Fig. 1B**). This
46
47 150 complex was interpreted as a sedimentary accretionary wedge composed of oceanic sediments
48
49
50 151 and accreted slices of oceanic lithosphere (Lafay et al., 2013; Lagabrielle et al., 1985). The
51
52 152 metamorphic grade increases eastwards, from temperature < 350 °C and pressure < 1.1 GPa,
53
54
55 153 to *P-T* conditions pertaining to the blueschist-facies conditions (up to 480 °C and $P > 1.2$
56
57 154 GPa; Agard et al., 2001). The Queyras ophiolite crops out as scattered large olistoliths within
58
59 155 the metasedimentary Schistes Lustrés: the ophiolite bodies preserve the original internal
60
61
62
63
64
65

156 structure and stratigraphy, enabling reconstruction of their oceanic history (Tricart and
1 157 Lemoine, 1991). Within each body, three major components of the oceanic lithosphere can be
2
3 158 distinguished; from bottom to top these are (i) an ultramafic sequence of serpentinitized
4
5
6 159 mantle-derived peridotites, locally crosscut by Late Triassic gabbro intrusions (Carpena and
7
8 160 Caby, 1984), (ii) a discontinuous basaltic layer of tholeiitic pillow basalts, and (iii) a
9
10
11 161 sedimentary pelagic cover represented by the Schists Lustrés complex. Where the basaltic
12
13 162 sequence is missing, the ultramafic and the sedimentary rocks can be directly in contact
14
15
16 163 (Tricart and Lemoine, 1991). The ophicarbonates are on top of the ultramafic sequence
17
18 164 and can be subdivided into groups of tectonic (OCI) and sedimentary (OCII) origin. The first
19
20
21 165 type is characterized by a dense network of calcite veins and fractures formed by tectonic
22
23 166 extension and hydraulic fracturing; the OCII type derives from in-situ reworking of OCI, of
24
25 167 serpentinites and/or basaltic materials forming clasts in a micrite matrix (e.g., Lemoine et al.,
26
27
28 168 1987). The presence of ophicarbonates is interpreted as representing exposure of mantle
29
30 169 to seawater on the ocean floor (Tricart and Lemoine, 1991). The ophicate samples
31
32
33 170 analyzed in this study (CU samples in **Fig. 1B**) experienced blueschist-facies *P-T* conditions
34
35 171 (325 – 375 °C and 1.1 – 1.4 GPa; Michard et al., 2004).

36
37 172

40 173 *2.2.3 Voltri Massif*

42 174 The ophiolitic Voltri Massif is a blueschist- to eclogite-facies complex of Jurassic
43
44
45 175 oceanic lithosphere composed of serpentinites hosting gabbro- and basalt-derived eclogite and
46
47 176 metaroddingite. This sequence is associated with high-*P*-metamorphosed oceanic sediment, i.e.
48
49
50 177 calc- and mica-schists (referred to as Schistes Lustrés) interlayered with metabasalts and
51
52 178 cherts (e.g., Chiesa et al., 1975). Remnants of sub-continental lithospheric mantle are well-
53
54
55 179 exposed in the Erro-Tobbio metaperidotite unit, representing the pre-Alpine rifting and ocean-
56
57 180 floor alteration followed by subduction and metamorphism at eclogite-facies *P-T* conditions
58
59 181 (Hermann et al., 2000; Hoogerduijn Strating et al., 1993; Scambelluri et al., 1995, 1991;

182 Visser et al., 1995, 1991). Peak metamorphic *P-T* estimates for the Voltri Massif are about
1 183 450 – 500 °C and 1.3 – 1.7 GPa (Cimmino et al., 1979; Federico et al., 2004; Messiga and
2
3 184 Scambelluri, 1991), conditions that produced metamorphic olivine + antigorite in
4
5
6 185 serpentinites, garnet + omphacite + rutile in eclogite and high-Si-bearing phengite + garnet in
7
8 186 metasedimentary rocks. Field and geochemical evidence (Cannaò et al., 2016; Federico et al.,
9
10
11 187 2007; Scambelluri and Tonarini, 2012), together with numerical modelling (Malatesta et al.,
12
13 188 2012), suggests a complex history for the Voltri Massif during prograde and retrograde
14
15
16 189 evolution along the slab-mantle interface.

17
18 190 The ophicarbonates of the Voltri Massif crop out in several localities (**Fig. 1**) and
19
20
21 191 were first described by Cortesogno et al. (1981, 1980). These rocks consist of carbonate
22
23 192 mineral phases (calcite, dolomite and/or magnesite) coexisting with antigorite and, locally,
24
25 193 metamorphic olivine. These rocks are interpreted as the metamorphic counterparts in the non-
26
27
28 194 subducted oceanic ophicarbonates of the Northern Apennines ophiolites, with grades ranging
29
30 195 from greenschist-, to blueschist-, to eclogite-facies. Recently, Scambelluri et al. (2016)
31
32
33 196 described in detail the evolution, metamorphic reactions, and C and O isotope compositions at
34
35 197 an outcrop within the Voltri Massif, highlighting the high potential of serpentinite for
36
37
38 198 sequestering C and thus influencing the deep C cycle. The samples from the Voltri Massif
39
40 199 analyzed in this study are from two localities representing ophicarbonates affected by the
41
42 200 eclogite-facies metamorphism: La Pesca (Scambelluri et al., 2016; LP13 EOC samples) and
43
44
45 201 Sant’Anna (SA samples).

50 203 **3. Petrography and microstructures**

51
52 204 The ophicate samples presented here retain evidence of complex polyphase
53
54 205 histories. Here, we describe the key features of representative ophicate samples from
55
56
57 206 each locality: for the Northern Apennine, we retain the classification of the ophicarbonates of
58
59 207 tectonic-hydrothermal (OCI) and sedimentary (OCII) origin initially proposed by Lemoine et
60
61
62
63
64
65

208 al. (1987). Also, we describe the oceanic serpentinite exposed in the Northern Apennine,
1 209 regarding it as the starting material (protoliths) for the higher-grade ophicarbonates.

2
3 210

6 211 ***3.1 Oceanic Northern Apennine Ophicarbonates***

8 212 *Serpentinite protolith rocks*

10 213 The ultramafic protoliths of the oceanic ophicarbonates are represented by highly (90%)
11 214 to fully (100%) serpentinitized mantle peridotites. In these rocks, static pseudomorphic
12 215 replacement led to formation of mesh serpentine + magnetite textures after mantle olivine and
13 216 bastite after mantle pyroxenes in which traces of the former pyroxene cleavage are still
14 217 recognizable. The medium grain size of the pseudomorphs and the isotropic texture suggest
15 218 an original harzburgite for these ultramafic rocks. The sample collected in this study does not
16 219 display evidence for deformation, but high-*T* shear domains are described in the literature for
17 220 the serpentinite basement (Treves and Harper, 1994).

18 221

20 222 *Ophicarbonates of tectonic and hydrothermal origin (OCI)*

22 223 The ophicarbonates of tectonic and hydrothermal origin (OCI) contain several
23 224 generations of carbonate veins overprinting the serpentinitized precursor. Calcium carbonate is
24 225 the most widespread mineral, ubiquitous in these rocks at this stage. Samples can display
25 226 variably extensive carbonation of the starting serpentinite during the hydrothermal activity.
26 227 The amounts of vein-related calcite can range from few modal % calcite (e.g., ZRL 15-3) to
27 228 more than 80 % (e.g., MNT 13-5) of the host rock. The host serpentinite has the texture of a
28 229 jigsaw puzzle breccia with clasts ranging in size from the outcrop scale (m in size) to hand-
29 230 sample size (few cm)- and to mm-scale. The ultramafic clasts also display varying extents of
30 231 carbonation, from less than 20% (ISC 13-1) to 90% (ZRL 13-1) in volume.

31 232 The ultramafic clasts correspond to fully serpentinitized peridotites, which do not
32 233 preserve olivine and which rarely preserve relict mantle pyroxene and spinel partially

33
34
35
36
37
38
39
40
41
42
43
44
45
46
47
48
49
50
51
52
53
54
55
56
57
58
59
60
61
62
63
64
65

234 converted to magnetite. The clasts of the host serpentinite are heterogeneous in size and
1 235 polygonal in shape, with sub-angular to angular edges. Each clasts preserves a record of the
2
3 236 original undeformed and deformed structure of the serpentinitized mantle peridotite host. The
4
5
6 237 monotonous chrysotile + magnetite assemblage of the pure serpentinite clasts is locally
7
8 238 accompanied by formation of chlorite, talc and tremolite. Near the calcite hydrothermal veins,
9
10
11 239 the serpentinite clasts unaffected by carbonation and preserving mantle pyroxene relics show
12
13 240 evidence of infiltration in the form of small- to medium- sized calcite veinlets.

14
15 241 The serpentinite clasts are affected by varying degrees of carbonation: from minor
16
17
18 242 overgrowth by neoblastic fine-grained calcite to reddish clasts showing pervasive to full
19
20 243 carbonation associated with oxidation. This carbonation represent a key feature of such
21
22
23 244 hydrothermally-altered oceanic ophicarbonates: full carbonation of the ultramafic silicate
24
25 245 clasts concurs with formation of variably abundant hematite after magnetite. Replacement by
26
27
28 246 calcite of serpentine from the core of the mesh texture and along cleavage of the former
29
30 247 pyroxene by calcite occurs in nearly all oceanic samples. Locally, along the cleavages of
31
32
33 248 serpentinitized pyroxenes, trails of small green andraditic garnet crystals are intergrown with
34
35 249 serpentine and calcite (**Fig. 2C**). In samples where the carbonation has been quite extensive,
36
37
38 250 the serpentinite clasts are entirely replaced by fine-scale calcite grains and a film of hematite
39
40 251 grows along the border, giving them a ghost-like texture (**Fig. 2A, B**). Interestingly, the full
41
42 252 carbonation of the ultramafic silicate clasts appears to be associated with the formation of
43
44
45 253 abundant hematite (**Fig. 2A, B**), suggesting that the Fe^{2+} released by the carbonated silicates
46
47 254 was converted to Fe^{3+} thus stabilizing hematite due to increased oxidizing conditions.

48
49 255 The last brittle deformation event recorded by these rocks is represented by the
50
51
52 256 formation of calcite veins that crosscut all previous structures. Calcite is coarse-grained and
53
54 257 shows euhedral habit and, typically, twinning. Talc is observed in drusy textures commonly in
55
56
57 258 the core of the veins, seemingly representing as the last precipitates. In some samples, calcite
58
59 259 is replaced by talc aggregates (**Fig. 2D**).

60
61
62
63
64
65

1 261 *Sedimentary ophicarbonates (OCII)*

2
3 262 These rocks display a sedimentary breccia-like texture with clasts consisting of
4
5
6 263 serpentinites or of reworked OCI. The sedimentary OCII clasts typically display angular
7
8 264 edges and widely varying grain size from several millimeters to few hundreds of micrometers.
9
10
11 265 The mineral assemblage of the clasts, as in the OCI, consists of serpentine, magnetite, chlorite,
12
13 266 talc and minor tremolite. Based on the extent of carbonation and oxidation, two types of
14
15 267 sedimentary breccias can be identified: (i) samples SG 15-4 and MNT 15-2, showing minor
16
17
18 268 and abundant carbonation and oxidation, respectively, and (ii) sample SG 15-2, showing
19
20 269 intermediate amounts of carbonation and oxidation.

21
22
23 270 The green colour of ophicarbonate SG 15-4 reflects the high modal abundance of
24
25 271 hydrous silicate minerals still preserved in the rock. The textures of the serpentinite clasts
26
27
28 272 preserve the mantle mineral domains; however, some clasts with complex texture likely
29
30 273 derive from pre-existing serpentine veins. The matrix calcite range from micritic to sparry, the
31
32
33 274 latter occurrence type showing twinning. The sedimentary structures are cut by calcite veins
34
35 275 showing, from rim to core, a change from botryoidal to irregular blocky textures (**Fig. 2E**).

36
37 276 The ophicarbonate sample MNT 15-2 shows an intense degree of carbonation and
38
39
40 277 oxidation, with a reddish color due a large amount of hematite (**Fig. 2F**). In sample SG 15-2,
41
42 278 only a few % of the clasts still preserve the original serpentinite composition, while
43
44
45 279 widespread ghost-like textures derive from full replacement of former silicate minerals by
46
47 280 fine-grained calcite. Locally, the clasts are composed of single crystals of calcite, probably
48
49
50 281 derived from reworking of the OCI and associated hydrothermal calcite veins. The matrix of
51
52 282 sample MNT 15-2 consists mainly of medium- to fine-scale (to microcrystalline) grains of
53
54 283 anhedral calcite with lobate and irregular intercrystalline boundaries. Along the contact
55
56
57 284 between the clasts and the matrix, calcite grows as cement crusts typically forming
58
59 285 gravitational beard-like patterns.
60
61
62
63
64
65

3.2 Subduction-related ophicarbonates

Pumpellyite-actinolite-facies ophicarbonates

Samples PL 13-1 and PL 13-2 display two texturally different types of micro-domains indicating multiple stages of recrystallization of calcite grains. The first micro-domain consists of coarse- to medium-sized grains of calcite (1) showing development of a second generation of twin lamellae cutting at high angles the earlier-formed generation and affected by growth of twin-free calcite grains. The coarse calcite (1) is cut by shear zones that represent the second type of micro-domain observed in these samples. The shear zones consist of medium- to fine- grained, un-twinned calcite (2) irregular in shape and with complex grain boundaries. Along the shear zones, calcite (1) is partially recrystallized and becomes elongated and re-oriented coherently into the shear zone orientation (**Fig. 3A**). Both samples (PL 13-1 and PL 13-2) also contain 10-20 volume % serpentinite clasts ranging in size from several centimetres to a few millimetres. In general, the largest clasts are broken into smaller pieces when embedded and displaced along the shear-zones as sigmoidal porphyroclasts. The serpentinite clasts consist of magnetite and antigorite showing tabular and interlocking textures grown at the expense of mesh-like lizardite/chrysotile. In shear zones, thin dark films of antigorite are interlayered with the calcite (2), giving to the rock an S-C like texture. The serpentinite clasts in these samples thus derive from an early stage of oceanic serpentization and carbonation.

A key feature pertaining to these samples is the replacement of antigorite within the clasts by neoblastic calcite. Calcite overgrowths occur along the contacts between antigorite and calcite within the shear zones and inside the various serpentinite clasts (**Fig. 3B**). These textures indicate that replacement of serpentinite by calcite was due to syn-deformation infiltration by carbonic fluids.

312 *Blueschist-facies ophicarbonates*

1 313 Samples CU3 and CU 13-1 represent ophicarbonates re-equilibrated at blueschist-facies
2
3 314 *P-T* conditions. CU3 consists of coarse serpentinite clasts in a coarse-grained calcite matrix.
4
5
6 315 In the clasts, antigorite overgrows earlier serpentine minerals and, in the majority of the clasts,
7
8 316 the original serpentinite texture is cross-cut and overgrown by networks of calcite-bearing
9
10
11 317 veins. The coarse-grained matrix-forming calcite is anhedral and shows corroded grain
12
13 318 boundaries, undulose extinction, and abrupt change in the twin growth, features that together
14
15 319 represent deformation during crystallization. The calcite grains formed along the contacts
16
17
18 320 with the serpentinite clasts and within the fracture network (**Fig. 3C**) display elongate textures
19
20 321 suggesting syn-deformation crystallization.

22
23 322 Sample CU 13-1 shows the development of carbonate-rich shear zones alternating with
24
25 323 domains with abundant serpentinite clasts. The shear zone textures are quite similar to those
26
27
28 324 in samples PL 13-1 and PL 13-2 and are characterized by re-orientation of calcite and
29
30 325 serpentinite clasts along the shear foliation and by crystallization of neoblastic calcite
31
32 326 emanating from the grain boundaries of former calcite (**Fig. 3D**). Deformation within the
33
34
35 327 shear zones leads to fracturing of the serpentinite clasts, grain size reduction, and uniform
36
37 328 orientation of the antigorite flakes. Within the shear zones, the matrix calcite is very fine-
38
39
40 329 grained (maximum 100 μm) and shows heterogranular and hypidiotopic fabric typical of
41
42 330 dynamic recrystallization and imparting a marble-like texture. The lack of twin lamellae in
43
44
45 331 this type of calcite suggests an increase in the *T* conditions with respect to that experienced by
46
47 332 the coarse-grained calcite crystals.

48
49 333

50
51
52 334 *Eclogite-facies ophicarbonates*

53
54 335 Samples from the La Pesca locality (LP13 EOC1 and LP13 EOC3) display an antigorite
55
56
57 336 + calcite + magnetite (\pm hydro-garnet in sample LP13 EOC1) mineral assemblage. As in the
58
59 337 oceanic samples, garnet forms along the cleavages of the serpentinitized pyroxene and, locally,
60
61
62
63
64
65

338 around magnetite pods displaced along the main foliation (**Fig. 3E**). As often occurs in
1 339 serpentinite, the magnetite pods may derive from oceanic alteration and recrystallization of
2
3 340 Cr-rich mantle spinel. The main difference between the two La Pesca samples is the strong
4
5 341 deformation affecting LP13 EOC3, a texture similar to that of samples CU 13-1 and PL 13-
6
7
8 342 1/2. Despite the textural similarity to CU 13-1 and PL 13-1/2, deformed calcite in sample
9
10 343 LP13 EOC3 is much finer-grained and contains more equigranular fabrics and hypidiotopic to
11
12 344 idiotopic crystals. Sample LP13 EOC1 largely consists of calcite veins cutting the entire rock
13
14
15 345 structure and suggesting late (subduction-related?) infiltration of C-bearing fluids along
16
17 346 fractures.

18 347 The S. Anna ophicarbonates are the only samples showing dolomite and magnesite
19
20 348 associated with antigorite, magnetite, minor chlorite, and diopside. In these rocks, coarse
21
22 349 porphyroclastic magnesite occurs within the foliation produced at high-*P* conditions, probably
23
24 350 as the result of tectonic dismemberment of former veins (sample SA 15-8). An interesting
25
26 351 feature of this magnesite is the presence of primary and pseudo-secondary fluid inclusions
27
28 352 (**Figs. 3G, 3H**) showing tabular shapes, variable size (from 20 to few μm) and infilling by
29
30 353 liquid + gas. Occasionally, small aggregates of Ti-clinohumite are present and associated with
31
32 354 the magnesite grains. Magnesite is partially replaced by dolomite and calcite along contacts
33
34
35 355 with antigorite and, concurrent with this replacement, acicular tremolite was formed after
36
37 356 antigorite.

38 357 Sample SA 15-1 shows micro-scale shear zones similar to those found in the other
39
40 358 subduction-related samples: in such sheared domains, dolomite is overgrown by calcite,
41
42 359 antigorite and minor chlorite likely related to retrograde deformation. Though high-*P*
43
44 360 conditions were reached in the S. Anna area, as described in literature, no evidence of
45
46 361 metamorphic olivine has been found in the samples investigated here. However, we interpret
47
48 362 the dolomite + antigorite + diopside assemblage (**Fig. 3F**) as representing high-*P* conditions
49
50
51
52
53
54
55
56
57
58
59
60
61
62
63
64
65

363 comparable with those of the ophicarbonates from the Zermatt-Saas Unit (Chatillon area, W.
1 364 Alps), the latter peak-metamorphosed at 1.4 GPa and 450-550 °C (Driesner, 1993).

2
3 365

4 366 **4. Methods**

7 8 367 *4.1 Bulk rocks*

9
10 368 Whole rock major element analyses were performed at ActLabs Ltd. using a fusion
11
12
13 369 technique employing a Li-metaborate/tetraborate fusion digested in a weak nitric acid and
14
15 370 measured by ICP-OES. Accuracy and precision are estimated as better than 1%. Loss on
16
17
18 371 ignition (LOI) was determined by weight difference following ignition of samples in a
19
20 372 furnace. The amount of CO₂ was determined by calcimetry at the IGG-CNR (Pisa, Italy) by
21
22
23 373 reacting small aliquot of sample (about 0.3 g) with HCl, and measuring the release of CO₂
24
25 374 from carbonates through the volume of water shifted in a graduated cylinder. The
26
27
28 375 concentration is then calculated using a calibration line. The CO₂ measured from sample
29
30 376 containing the less-reactive magnesite in the assemblage (i.e., SA 15-8) may be
31
32
33 377 underestimated. The amount of H₂O was estimated by the simple difference between LOI and
34
35 378 CO₂ contents for each sample.

36
37 379 Trace element concentrations (except for B) were accomplished using an Agilent 7700x
38
39
40 380 quadrupole ICP-MS at Géosciences Montpellier (AETE-ISO facility, Montpellier, France)
41
42 381 following the procedure described in Godard et al. (2000) and Ionov et al. (1992). Boron
43
44
45 382 concentrations for all samples were determined by isotope dilution using the NIST SRM 982
46
47 383 spike in a single collector VG Isomass 54E positive thermal ionization mass spectrometer (P-
48
49
50 384 TIMS) running in dynamic mode at the IGG-CNR (Pisa, Italy).

51
52 385

53 54 386 *4.2 Mineral compositions*

55
56
57 387 Major element mineral compositions were measured at the Department of Earth
58
59 388 Sciences, University of Milano (Italy), using the electron microprobe JEOL Superprobe 8200.

60
61
62
63
64
65

389 The analyses were conducted with a WDS system at 15.0 kV, 5 nA for the electron beam and
1 390 1 μm beam size. We used natural silicate standards (the numbers refer to the international
2
3 391 standards): Mg on olivine 153, Fe on fayalite 143, Na on omphacite 154, Ti on ilmenite, Mn
4
5
6 392 on rodonite, K on k-feldspar 113, Al and Ca on anorthite 137, Cr on metallic/pure Cr and Si
7
8 393 on wollastonite.

10
11 394 Mineral trace element concentrations were determined at the University of Bern by laser
12
13 395 ablation, using a Geolas Pro 2006 193 nm ArF excimer laser coupled to an Elan DRC-e ICP-
14
15 396 MS instrument (LA-ICP-MS). Analytical strategies, data reduction and instrument
16
17
18 397 optimization procedures closely follow those reported by Spandler et al. (2011) and Pettke et
19
20 398 al. (2012). Beam sizes were as large as possible (up to 160 μm diameter) to lower the
21
22
23 399 detection limits, calculated using the stringent formulation in Pettke et al. (2012). External
24
25 400 standardization was against the GSD-1D basalt glass, employing the values cited in Peters
26
27
28 401 and Pettke (2017) and the GeoRem data base (Jochum et al., 2005). Data reduction employed
29
30 402 SILLS (Guillong et al., 2008), and the sum of all measured element oxides (total oxides, i.e.,
31
32
33 403 100 wt.% minus LOI; e.g., Halter et al., 2002) was used as the internal standard for
34
35 404 quantification. Due to the lack of data for $\text{Fe}^{3+}/\text{Fe}^{2+}$, total Fe was calculated as FeO. Ablation
36
37
38 405 rates were turned to c. 0.08 μm per pulse via attenuation of the laser output beam; the laser
39
40 406 repetition rate was 10 Hz. Measurement accuracy and precision were monitored by analysing
41
42 407 SRM612 glass from NIST as an unknown, and the data mostly agree to within 5% of the
43
44
45 408 reference values (**Supplementary Table A3**).

49 50 410 *4.3 Isotopic analyses*

51
52 411 The samples were analyzed for $\delta^{13}\text{C}$ and $\delta^{18}\text{O}$ at the Department of Earth and
53
54
55 412 Environmental Sciences, Lehigh University (USA), using a Finnigan MAT 252 gas mass-
56
57 413 spectrometer coupled with a GasBench II system, applying the methods described by Cook-
58
59
60 414 Kollars et al. (2014) and Collins et al. (2015). We analyzed bulk rocks as well as more pure
61
62
63
64
65

415 carbonates from different textural settings sampled by micro-drilling, using tungsten carbide
1 416 bits with diameter of 1 and 2 mm. Calcite, dolomite or magnesite was reacted at 72 °C for 30
2
3 417 min, 3 or 6 hours, respectively, with 0.2 mL 100% phosphoric acid (H₃PO₄) in order to
4
5 418 release CO₂, according to the methods of McCrea (1950), Paul and Skrzypek (2007), and
6
7
8 419 Sharma et al. (2002). All data are presented in standard delta(δ)-notation, reported relative to
9
10 420 VPDB and VSMOW for δ¹³C and δ¹⁸O, respectively. Regular analyses of an in-house
11
12 421 standard and the international standard NBS-19 allowed monitoring and correction of the data,
13
14
15 422 resulting in a standard deviation (1σ) of ~ 0.2‰ for both δ¹³C and δ¹⁸O.
16

17
18 423 Strontium isotope analyses were performed using a Finnigan MAT 262 multicollector
19
20 424 mass-spectrometer (at the IGG-CNR, Pisa, Italy), operated in dynamic mode, after ion-
21
22 425 exchange purification through Sr-spec resin. Measured ⁸⁷Sr/⁸⁶Sr ratios were normalized to
23
24
25 426 ⁸⁶Sr/⁸⁸Sr = 0.1194. Replicate analyses of NIST SRM 987 (SrCO₃) standard gave an average
26
27 427 value of 0.710207 ± 13 (2SD, n = 5). Published values are adjusted to ⁸⁷Sr/⁸⁶Sr = 0.710250.
28
29 428 Strontium blanks were about 0.3 ng, which are negligible given the Sr concentrations in the
30
31
32 429 samples analyzed in this study.
33

34
35 430

36 37 431 **5. Results**

38 39 432 *5.1 Bulk rock major and trace element concentrations*

40 433 The major element whole-rock concentrations of the samples are reported in **Table 1**.
41
42 434 The compositions of ophicarbonates are linked to the proportion of ultramafic and carbonate
43
44 435 component present: here, the composition of a pure serpentinite and an oceanic limestone
45
46 436 (MNT 15-1 and ZRL 15-7, respectively) were considered as the end-members for all of the
47
48 437 ophicarbonate rocks that were investigated. The major element compositions of OCI and
49
50 438 OCII ophicarbonates plot along a linear array in a CaO, MgO and SiO₂ diagram, as do the
51
52 439 subduction-related ophicarbonates. Similar variations in CO₂ and H₂O with respect to MgO
53
54 440 and CaO are displayed for all ophicarbonates, with rocks showing more evidence of
55
56
57
58
59
60
61
62
63
64
65

441 recrystallization during subduction processes (e.g. PL 13-2, CU 13-1 and LP13 EOC3)
1 442 plotting near the CO₂-rich end-member (**Fig. 4**). Sample SA 15-8, which contains magnesite,
2
3 443 has a slightly higher MgO concentration and a lower CaO concentrations than the other
4
5
6 444 subduction-related ophicarbonates (**Fig. 4**).

7
8 445 Trace element whole-rock compositions of the samples are reported in **Table 1** and in
9
10
11 446 **Fig. 5**. The pure serpentinite sample MNT 15-1 shows low REE concentrations with respect
12
13 447 to primitive mantle values (PM, McDonough and Sun, 1995) and a negligible negative Eu
14
15 448 anomaly. The strong light (L)REE depletion relative to concentrations of medium (M)REE
16
17
18 449 and heavy (H)REE ($La_N/Nd_N = 0.15$; $Sm_N/Ho_N = 0.36$; $Er_N/Lu_N = 0.81$) suggests a depleted
19
20 450 harzburgite protolith. The limestone sample ZRL 15-7 is enriched in LREE to MREE whereas
21
22
23 451 the HREE are almost flat ($La_N/Nd_N = 2.63$; $Sm_N/Ho_N = 2.07$; $Er_N/Lu_N = 1.19$). This sample
24
25 452 shows a negative Eu anomaly ($(Eu/Eu^*)_N = 0.85$).

26
27 453 OCI rocks have complex REE patterns, showing varying degrees of enrichment in
28
29
30 454 LREE ($La_N/Nd_N = 1.76 - 3.80$) and relative depletion in MREE and HREE but with similar
31
32
33 455 Sm_N/Ho_N and Er_N/Lu_N ratios (0.35 and 0.82, respectively) compared to pure serpentinite
34
35 456 sample. Only sample ISC 13-1 shows a higher concentration of MREE ($Sm_N/Ho_N = 0.89$). Of
36
37
38 457 the OCI samples, ZRL 13-1 is the only rock with a positive Eu anomaly. The REE patterns of
39
40 458 the sedimentary ophicarbonates (OCII) are comparable to those of the OCI rocks, with the
41
42 459 exception of sample SG 15-2 that is far more enriched in all REE ($La_N/Nd_N = 1.78$; Sm_N/Ho_N
43
44
45 460 $= 0.89$; $Er_N/Lu_N = 0.93$), although the concentrations are all below those of primitive mantle
46
47 461 to which they are normalized. All ophicarbonates have negative Ce anomalies, with $(Ce/Ce^*)_N$
48
49
50 462 ranging from 0.12 to 0.80.

51
52 463 Pumpellyite-actinolite-facies ophicarbonates (PL 13-1 and 2) are homogeneous in their
53
54
55 464 abundances of REE with concentrations far lower than those of the primitive mantle. Overall,
56
57 465 their REE concentrations differ greatly from those of the oceanic ophicarbonates. More
58
59 466 specifically, they show enrichment in LREE ($La_N/Nd_N = 2.77$) without negative Ce anomalies,
60
61
62
63
64
65

467 relatively flat MREE and HREE patterns ($\text{Sm}_N/\text{Ho}_N = 1.09$; $\text{Er}_N/\text{Lu}_N = 0.89$), and positive Eu
1 468 anomalies ($(\text{Eu}/\text{Eu}^*)_N = 1.81$).

2
3 469 Blueschist-facies ophicarbonates CU3 and CU 13-1 have similar REE patterns,
4
5
6 470 differing only in their HREE concentrations, the latter lower in sample CU 13-1 ($\text{Er}_N/\text{Lu}_N =$
7
8 471 2.50 against 1.05). They display a slight enrichment in LREE ($\text{La}_N/\text{Nd}_N = 0.74 - 0.48$), slight
9
10
11 472 depletion in MREE ($\text{Sm}_N/\text{Ho}_N = 1.25 - 1.35$) and positive Eu anomalies ($(\text{Eu}/\text{Eu}^*)_N = 1.46 -$
12
13 473 1.51). For these samples, all PM-normalized REE concentrations fall between 0.1 and 1.

14
15 474 The eclogite-facies ophicarbonate LP13 EOC1 shows LREE enrichment ($\text{La}_N/\text{Nd}_N =$
16
17
18 475 2.24) with a strong negative Ce anomaly, and enrichment of MREE relative to HREE
19
20
21 476 ($\text{Sm}_N/\text{Lu}_N = 0.54$). Europium shows a slight negative anomaly. Sample LP13 EOC3 shows a
22
23 477 similar REE pattern ($\text{La}_N/\text{Nd}_N = 1.18$ and $\text{Sm}_N/\text{Lu}_N = 0.62$), but about 1 order of magnitude
24
25 478 lower on the normalized plot. The negative Ce anomaly is less pronounced and Eu shows a
26
27
28 479 slight positive anomaly. The eclogite-facies sample SA 15-1, from the S. Anna locality in the
29
30 480 Voltri Massif, displays a low La_N/Nd_N ratio (0.70) and shows MREE enrichment relative to
31
32
33 481 HREE ($\text{Sm}_N/\text{Lu}_N = 3.64$). The magnesite-bearing ophicarbonate (SA 15-8) shows enriched
34
35 482 REE concentrations, relative to primitive mantle values, with LREE lower than MREE and
36
37
38 483 HREE ($\text{La}_N/\text{Lu}_N = 0.33$) and almost flat HREE ($\text{Er}_N/\text{Lu}_N = 0.92$). Both SA 15-1 and SA 15-8
39
40 484 show negative Eu anomalies.

41
42 485 The primitive mantle-normalized (PM, McDonough and Sun, 1995) trace elements
43
44
45 486 concentrations of the serpentinite end-member (**Fig. 5C**) are similar to those of seafloor
46
47 487 serpentinites imparted by interaction with seawater-derived fluids. These similarities include
48
49
50 488 enrichment in B in (up to 100 times PM) and positive anomalies in Li, Pb, As, Sb and Sr, but
51
52 489 always at concentrations lower than those of the primitive mantle. Cesium and Rb
53
54
55 490 concentrations are below detection limits and Ba, U and Th concentrations also are very low.

56
57 491 Carbonation processes lead to varying degrees of enrichment in LILE and fluid-mobile
58
59 492 elements (FME; e.g., As, Sb, U, Sr and Li) in the oceanic ophicarbonates OCI and OCII (**Fig.**
60
61
62
63
64
65

493 **5C)**. Similarity in the extents of enrichment in LILE, B, U, Th, Pb and Li is common for the
1 494 subduction-related ophicarbonates (**Fig. 5D**). The trace element compositions of the eclogitic
2
3 495 samples are comparable to those of the other subduction-related ophicarbonates, with the
4
5
6 496 main differences being their higher Pb, As and Sb concentrations. Niobium and Ta
7
8 497 concentrations in sample SA 15-8 are near primitive mantle values whereas the concentrations
9
10
11 498 of these elements in all other samples are very low (between 0.002 and 0.1 normalized to PM
12
13 499 values).

14
15 500

18 501 *5.2 Mineral chemistry and in situ trace element concentrations*

20 502 Major element compositions of representative analyses of minerals in each sample are
21
22
23 503 reported in the **Table 2** and **3** and in the **Supplementary Table S1** and a detailed description
24
25 504 of the chemistry of the rock-forming minerals is reported in the **Supplementary Material 1**.
26
27
28 505 Briefly, the serpentine from oceanic and subduction-related ophicarbonates shows major
29
30 506 element composition similar to that of serpentine in the pure serpentinite sample characterized
31
32
33 507 by high MgO and SiO₂ contents and varying amounts of TiO₂, Al₂O₃ and Cr₂O₃ related to the
34
35 508 mantle mineral that was replaced (i.e., olivine or pyroxenes). Calcium-carbonate (CaCO₃) is
36
37
38 509 the dominant component of the carbonates in all oceanic and subduction-related
39
40 510 ophicarbonates (> 96%), except in eclogitic samples SA 15-8 and SA 15-1. The latter two
41
42 511 samples contain magnesite (MgCO₃ > 82% and FeCO₃ < 18%) and dolomite (with a Ca/Mg
43
44
45 512 ratio near 1.2) as the most abundant carbonate minerals.

47 513 The *in-situ* trace element compositions of serpentines and carbonates from the studied
48
49
50 514 samples are reported in **Table 2**, **Table 3**, and in **Figure 6**. When normalized to the primitive
51
52 515 mantle values (**Fig. 6A**), the trace element patterns of serpentine minerals from oceanic
53
54
55 516 ophicarbonates show positive anomalies in Cs, U, B, As, Sb, Sr and Li, whereas other LILEs
56
57 517 and Th are depleted. Negative HFSE (High Field Strength Elements) anomalies also are
58
59 518 present. Compared to the trace element concentrations of the pure oceanic serpentines (grey
60
61
62
63
64
65

519 field in **Fig. 6A**), these serpentinites also are enriched in La with respect to Ce, compatible
1 520 with the bulk-rock data for OCI and OCII. As expected, calcite in the OCI and OCII samples
2
3 521 (**Fig. 6C**) mostly shows enrichment in Sr with scattered enrichments in Rb, Ba, B, La and Li.
4
5
6 522 Calcite from the less carbonated and less oxidized sample SG 15-4 has much higher U
7
8 523 concentrations than the calcite in the other samples. As for the serpentine minerals, La in
9
10
11 524 calcite is enriched relative to Ce (e.g., sample MNT 15-2, **Fig. 6C**).

13 525 Antigorite from subducted ophicarbonates (**Fig. 6B**) shows trace element concentrations
14
15 526 comparable to those of the oceanic samples, except for variable Sr anomalies, with the
16
17
18 527 concentrations in general lower than PM in the eclogitic samples and higher than PM in the
19
20 528 all other rocks. Notably, As and Sb concentrations in the SA 15-1 and SA 15-8 samples fall at
21
22
23 529 the upper limit of the oceanic field. In situ trace element analyses of the calcites in sample PL
24
25 530 13-2 revealed concentrations comparable to those of oceanic OCI (**Fig. 6D**). In contrast, the
26
27
28 531 calcites in the blueschist-facies ophicarbonates are depleted in Li and enriched in Pb and
29
30 532 MREE, relative to HREE, and show positive Eu anomalies (**Fig. 6D**) compared with calcite
31
32
33 533 from the oceanic ophicarbonates. Carbonates in the eclogitic samples from La Pesca show
34
35 534 trace element patterns comparable to those of oceanic ophicarbonates; however, they show
36
37
38 535 enrichment in W and Pb. Dolomite and calcite in sample SA 15-1 (S. Anna area) are
39
40 536 characterized by strong enrichment in LREE, Pb, Sr and MREE relative to HREE. Overall,
41
42 537 the concentrations of nearly all trace elements in calcite in this sample are one order of
43
44
45 538 magnitude higher than those in the dolomites. Magnesite in sample SA 15-8 show low
46
47 539 concentrations in all trace elements, with very low Sr contents, but with strong enrichment in
48
49
50 540 HREE relative to MREE and LREE.

52 541

54 542 *5.3 Isotope geochemistry*

57 543 *5.3.1 Carbon and oxygen isotope compositions of carbonates*

58
59
60
61
62
63
64
65

544 Whole-rock C and O isotope compositions of the carbonate in the ophicarbonates suite
1 545 analyzed here are listed in **Table 4**. The complete C and O isotope dataset for the micro-
2
3 546 drilled carbonates from each of the localities, itemized for texture and mineralogy, is provided
4
5
6 547 in the **Supplementary Table S2** and the Figure in **Appendix A1**.

8 548 The $\delta^{13}\text{C}$ of the oceanic carbonates ranges from about 0.0 to +3.0‰ (**Fig. 7A**), without
9
10 549 any significant difference between calcite replacing silicates or calcite in the veins (see the
11
12
13 550 Figure in **Appendix A1**). These results are compatible with previously published data for the
14
15 551 Bracco ophicarbonates (Collins et al., 2015; Schwarzenbach et al., 2013). Carbonate in veins
16
17
18 552 has $\delta^{18}\text{O}$ values ranging from +18.2 to +26.0‰, whereas values for carbonates within the
19
20 553 serpentinite clasts and from the matrix in sedimentary rocks are lower, forming a cluster of
21
22
23 554 +14.3 to 18.9‰ (**Fig. 7A**). The higher $\delta^{18}\text{O}$ values correspond to calcite from late-stage veins
24
25 555 (**Fig. 2D**).

27 556 Pumpellyite-facies ophicarbonates (**Fig. 7B**) show $\delta^{13}\text{C}$ within the range of the
28
29
30 557 Apennine ophicarbonates (from 0.0 to +1.5‰) and the $\delta^{18}\text{O}$ values form a tight cluster
31
32
33 558 ranging from +14.4 to +15.5‰. The blueschist-facies CU3 samples show similar $\delta^{13}\text{C}$ (+0.1
34
35 559 to +0.9‰) and $\delta^{18}\text{O}$ from +15.8 and +17.9‰, but sample CU13-1 has negative $\delta^{13}\text{C}$ value (-
36
37 560 2.7 to -1.1‰) and $\delta^{18}\text{O}$ ranging from +16.4 to +18.1‰. The range shown by the latter sample
38
39
40 561 is compatible with values obtained by Collins et al. (2015) for ophicarbonates and carbonated
41
42 562 metabasaltic rocks from the same area (**Fig. 7B**). Eclogitic sample LP13 EOC3 has $\delta^{13}\text{C}$
43
44
45 563 ranging from +0.7 to +1.4‰ and $\delta^{18}\text{O}$ from 14.1 to 15.7‰, whereas LP13 EOC1 shows
46
47 564 similar $\delta^{13}\text{C}$ (+0.8 to +1.6‰) but lower $\delta^{18}\text{O}$ ranging from +10.8 and +11.5‰ (**Fig. 7B**).
48
49
50 565 Other Voltri Massif ophicarbonates from the S. Anna locality are similar in their $\delta^{13}\text{C}$ (+0.4 to
51
52 566 +1.7‰) but slightly higher in their $\delta^{18}\text{O}$ (+11.6 to +12.7‰, **Fig. 7B**).

57 568 *5.3.2 Strontium isotope compositions*

58
59
60
61
62
63
64
65

569 Strontium isotope compositions were analyzed for whole-rocks (except for sample SA
1 570 15-1) and are listed in **Table 4** and are plotted in **Fig. 8**, against $\delta^{18}\text{O}$ and $\delta^{13}\text{C}$. The $^{87}\text{Sr}/^{86}\text{Sr}$
2
3 571 data for the Northern Apennines samples are reported for an initial time of 160 Ma, whereas
4
5
6 572 the measured $^{87}\text{Sr}/^{86}\text{Sr}$ ratio is reported for the subducted ophiicarbonates. This choice is based
7
8 573 on the fact that the extent of the Sr isotopic re-equilibration during subduction evolution is
9
10
11 574 uncertain. However, as reported in **Table 4**, the differences between measured values and
12
13 575 age-corrected Sr isotope compositions for the subducted-related samples (for the Voltri
14
15
16 576 Massif of 33 Ma, Rubatto and Scambelluri, 2003) is very small (within the analytical error)
17
18 577 due to the very low Rb/Sr of the samples.

19
20 578 The $^{87}\text{Sr}/^{86}\text{Sr}$ of the pure serpentinite end-member is 0.706929, which is compatible
21
22
23 579 with values for serpentinite formed at the oceanic floor during interaction with seawater at
24
25 580 Jurassic time (Jurassic seawater value = 0.7070; Jones et al., 1994). The limestone is
26
27
28 581 characterized by higher Sr isotope value of 0.707048 which is compatible with a re-
29
30 582 equilibration with Upper Cretaceous seawater (Jones et al., 1994) as proposed by Barbieri et
31
32
33 583 al. (1979). Ophiicarbonates of tectonic and sedimentary oceanic origins show $^{87}\text{Sr}/^{86}\text{Sr}$ ratios
34
35 584 similar to those of the pure serpentinite, ranging from 0.705746 to 0.706703. This range
36
37
38 585 confirms the Jurassic oceanic imprint of the ophiicarbonates due to interaction between
39
40 586 seawater-derived fluids in hydrothermal systems. The pumpellyite- and blueschist-facies
41
42 587 ophiicarbonates from Pietralavezzara and Ubaye show similar values ranging from 0.706383
43
44
45 588 to 0.706833. The only exception is for sample CU1 13-1 that displays a slight enrichment in
46
47 589 radiogenic Sr up to a value of 0.707530, well above the values for Jurassic and Cretaceous
48
49
50 590 seawater. The $^{87}\text{Sr}/^{86}\text{Sr}$ of sample LP13 EOC3 (0.706791) is comparable to that of oceanic
51
52 591 rocks, whereas the other eclogitic ophiicarbonates have far more radiogenic compositions:
53
54 592 sample LP13 EOC1 and SA 15-8 have $^{87}\text{Sr}/^{86}\text{Sr} = 0.708453$ and 0.709670 , respectively, and
55
56
57 593 calcite and dolomite separates from sample SA 15-1 have $^{87}\text{Sr}/^{86}\text{Sr} = 0.707969$ and 0.708130 ,
58
59 594 respectively.
60
61
62
63
64
65

6. Discussion

Carbon release to subduction fluids and the mobility of aqueous-carbonic fluids within slabs or along the slab-mantle interface are actively debated topics in considerations of the solid Earth deep C cycle (Ague and Nicolescu, 2014; Berner, 1998; Collins et al., 2015; Cook-Kollars et al., 2014; Dasgupta and Hirschmann, 2010; Epstein et al., 2019; Jaeckel et al., 2018; Kelemen and Manning, 2015; Piccoli et al., 2016; Poli et al., 2009; Poli, 2015; Scambelluri et al., 2016). In this debate, a few studies have considered the geochemical evolution of ophicarbonates by investigating either the C-O isotope compositions of carbonates (Collins et al., 2015; Driesner, 1993; Lafay et al., 2017; Scambelluri et al., 2016; Weissert and Bernoulli, 1984), or the radiogenic isotope and trace element compositions of bulk-rocks and of rock-forming minerals (Miller and Cartwright, 2000; Yamaguchi et al., 2012). Lacking have been studies combining field and petrographic observation, and petrologic work, with trace element concentrations and C, O, and Sr isotope compositions of oceanic and of subduction-zone ophicarbonates aimed at elucidating the geochemical evolution of carbonated serpentinite along the subduction interface. Such studies can build on previous work employing trace elements and Sr isotopes to trace fluid-infiltration in subducting ultramafic rocks (Cannaò et al., 2016, 2015; Harvey et al., 2014). The approach presented in this paper employs such an integration and offers new insight regarding the mechanism of C mobilization in convergent margins.

6.1 Textural and petrologic features

The oceanic ophicarbonates studied here retain serpentine \pm magnetite mesh and bastite textures referred to as replacement of former mantle olivine and pyroxenes, respectively (from t_0 to t_2 in **Fig. 9**). During tectonic fragmentation of the serpentinitized mantle, carbonation of the bedrock by circulating hydrothermal fluids and accumulation of

621 serpentine clasts in sedimentary-tectonic breccias strongly affected the upper part of the
1 622 ultramafic sequence (Schwarzenbach et al., 2013; Treves et al., 1995). Calcite formation after
2
3 623 the production of the mesh textures (**Fig. 2A**), and along the cleavage of pseudomorph
4
5 624 pyroxene, indicates that the mantle protolith was serpentinized prior to carbonation (t3 in **Fig.**
6
7
8 625 **9**). Calcite formation after serpentinization requires open-system Ca and CO₂ input by the
9
10
11 626 hydrothermal fluids and the release of Si, Mg and water (as hydroxyl molecules – OH) into
12
13 627 the fluid. Thermodynamic modelling suggests that serpentine replacement by carbonates
14
15 628 occurred at 100 °C and 50 MPa at a high activity of CO₂ (Klein and Garrido, 2011). This
16
17
18 629 modelling was confirmed by experimental work showing that formation of calcite or
19
20 630 magnesite after serpentinization of peridotite is related to the activity of Mg²⁺ in the fluid and
21
22
23 631 to the presence of relict mantle minerals (Grozeva et al., 2017). Serpentine carbonation can
24
25 632 deliver abundant Mg and Si into the hydrothermal system with a consequent increase of the
26
27
28 633 Mg/Ca and Si/Ca of the solutions. In the OCI and OCII ophicarbonates, the absence of Mg-
29
30 634 carbonates like dolomite and magnesite, and the only minor MgCO₃ component in the calcite,
31
32
33 635 indicates that the hydrothermal fluids reached Mg²⁺ saturation only after full consumption of
34
35 636 the aqueous CO₂. In fact, the last carbonation event led to formation of late-stage calcite and
36
37
38 637 talc-bearing veins (**Fig. 2D**). Talc crystallization in such late-stage veins reflects the chemical
39
40 638 evolution of hydrothermal fluids through time towards Mg- and Si-rich, and Ca- and CO₂-
41
42 639 depleted composition, and marks the end of the oceanic hydrothermal carbonation system (t4
43
44
45 640 in **Fig. 9**). **Figure 10** reports the results of thermodynamic calculations presented as an
46
47 641 activity-activity diagram (log(*a*SiO₂) vs. log(*a*CO₂)) simulating the oceanic carbonation of the
48
49
50 642 pure serpentinite sample MNT 15-1 at low *T* and *P*. The initial carbonation occurs at
51
52 643 log(*a*CO₂) values between -11.0 and -7.0 for a log(*a*SiO₂) between -5.0 and -1.8 (red line in
53
54
55 644 **Fig. 10**). In this ranges of log(*a*SiO₂) values, the complete carbonation of relicts of residual
56
57 645 mantle minerals (e.g., olivine and pyroxenes) precedes the carbonation of serpentine, the latter
58
59 646 occurring at log(*a*CO₂) of -6.0 to -5.0. This process is accompanied by release of H₂O (blue
60
61
62
63
64
65

647 line in **Fig. 10**). At high $\log(a\text{SiO}_2)$ values, talc becomes stable (above -1.8, see the green line
1 648 in **Fig. 10**) over carbonates for a $\log(a\text{CO}_2)$ greater than -6.5.

2
3 649 The OCI and OCII ophicarbonates showing the highest modal proportions of rocks-
4
5
6 650 forming carbonate also display abundant hematite grains in the carbonated silicate domains
7
8 651 and hematite rinds on carbonated clasts (**Fig. 2A, B**; t4 in **Fig. 9**). Overall, these features
9
10
11 652 indicate highly oxidizing condition during carbonation, as also suggested by the formation of
12
13 653 hydrous andradite-rich garnet in the bastite textures after former pyroxenes (**Fig. 2C**).

14
15 654 The above oceanic transformations created highly oxidized, hydrated, and carbonated
16
17
18 655 serpentinite reservoirs hosting up to 40wt% CO_2 (**Fig. 4**). Subduction of these rocks was
19
20
21 656 accompanied by deformation of the oceanic textures (Stöckhert, 2002) with displacement and
22
23 657 recrystallization of coarse oceanic calcite and serpentine along ductile shear zones (**Fig. 3**). At
24
25 658 this stage, deformation might have occurred under chemically closed- or open-system
26
27
28 659 conditions. The behaviour of these rocks during subduction can be revealed by textural
29
30 660 analysis and study of geochemical markers. With the exception of samples SA 15-1 and SA
31
32
33 661 15-8, the majority of the subducted ophicarbonates for which data are presented here display
34
35 662 antigorite + calcite as the main mineral assemblage. Their textures and mineral assemblage
36
37
38 663 could reflect an internal redistribution/recrystallization of minerals and elements inherited
39
40 664 from the oceanic stage. However, the pumpellyite- and the blueschist-facies samples are
41
42 665 characterized by growth of secondary calcite after the serpentinization of the porphyroclasts
43
44
45 666 displaced along the shear-zone foliation (**Fig. 3B**). The geometry of these clasts suggests syn-
46
47 667 tectonic carbonation of serpentine during early subduction stages. Experimental studies
48
49
50 668 showed that the solubility of calcite in H_2O -rich fluid increases with increasing P - T
51
52 669 conditions of the system (Caciagli and Manning, 2003), suggesting that the carbonation of the
53
54
55 670 serpentinite clasts may have resulted from *in-situ* carbonate dissolution followed by *in-situ*
56
57 671 carbonate precipitation. Assuming a closed system condition, the H_2O required to trigger
58
59 672 calcite dissolution may have been derived from the serpentinite clast itself as few wt.% of
60
61
62
63
64
65

673 H₂O is released during the serpentine phase transition at increasing *P-T* conditions (Schwartz
1 674 et al., 2013).

2
3 675 Additional textural evidence for C mobility during subduction is provided by the
4
5
6 676 occurrence of carbonate veins crosscutting the eclogite-facies ophicarbonates in the Voltri
7
8 677 Massif (LP EOC13-1). Another indication of open system behaviour and infiltration of C-
9
10
11 678 bearing fluids precipitating eclogite-facies magnesite veins is provided by the abundant fluid
12
13 679 inclusions hosted by porphyroclastic magnesite of sample SA 15-8. As shown in **Fig. 11D**,
14
15 680 and as discussed below, these inclusions shows significant enrichment in FME relative to the
16
17
18 681 concentrations in their magnesite hosts. This might be further evidence for infiltration of C-
19
20 682 bearing fluids external to the ophicarbonate host.

21
22
23 683 Taken together, the textures and other observations presented above, for distinct
24
25 684 domains in the ophicarbonates we investigated, provide a record of C mobilization over a
26
27
28 685 wide range of *P-T* conditions, beginning on the seafloor and during very early stages of
29
30 686 subduction.

31
32
33 687

34 35 688 *6.2 Bulk and in-situ trace element features*

36
37 689 It has been demonstrated that the serpentinization of the oceanic mantle rocks does not
38
39
40 690 strongly modify the REE composition of the peridotite protoliths (Deschamps et al., 2013 and
41
42 691 reference therein). The REE composition of the reference serpentinite MNT 15-1 thus
43
44
45 692 reasonably reflects its mantle protolith that is comparable to Internal Liguride (Liguria, Italy)
46
47 693 and Monte Maggiore (Corsica, France) peridotites (grey field in **Fig. 5A**; Rampone et al.,
48
49
50 694 2008, 1996). The similarity in the trace element composition of rock-forming serpentine from
51
52 695 MNT 15-1 (showing positive B anomaly and depletion in LILE and FME; grey field in **Fig.**
53
54 696 **6A**) with other oceanic serpentinites (e.g., Kodolányi et al., 2012) confirms that the alteration
55
56
57 697 process occurred in a marine environment. In contrast, the carbonation of oceanic
58
59 698 serpentinites significantly affects REE concentrations (**Fig. 5A**; Allen and Seyfried, 2005).

60
61
62
63
64
65

699 Accordingly, compared to serpentinite MNT 15-1, all of our oceanic ophicarbonates display
1 700 enrichments in La and variable depletion in Ce (**Fig. 5A**). The oxidation process that occurs
2
3 701 during carbonation, revealed by conversion of magnetite to hematite, also affects the
4
5 702 behaviour of Ce that, upon oxidized to Ce^{4+} , becomes incompatible in the serpentine and
6
7
8 703 carbonate. Cerium depletion is recorded by the bulk-rock and the mineral *in-situ* analyses of
9
10
11 704 most oceanic ophicarbonates (**Fig. 5A** and **6A**). The enrichment of Ba, B, Cs, U, Pb, As, Sb,
12
13 705 Sr, Li in the oceanic ophicarbonates and their rock-forming serpentine and carbonate can be
14
15 706 also linked to the carbonation and oxidation of these rocks (Andreani et al., 2014).
16
17
18 707 Enrichment of FME in serpentine may be explained by the alkaline conditions of the
19
20
21 708 hydrothermal environment increasing adsorption of these elements onto the serpentine
22
23 709 mineral structure. According to the experimental work by Lafay et al., (2016) the As and Sb
24
25 710 enrichments in serpentine (**Fig. 6A**) can be explained when considering that As^{5+} and Sb^{5+} are
26
27
28 711 favourably sequestered by serpentine minerals, compared with As^{3+} and Sb^{3+} , the latter which
29
30 712 are mobilized in the fluid phase and/or precipitate as Sb-Ni-accessory phases. For the
31
32
33 713 ophicarbonate calcite, the *in-situ* trace element concentrations are similar to those of
34
35 714 serpentine, at least for As that is variably enriched. Uranium is mostly enriched in calcite in
36
37
38 715 the less oxidized sample SG15-4, consistent with its high solubility at elevated oxygen
39
40 716 fugacity (e.g., Bailey and Ragnarsdottir, 1994; Keppler and Wyllie, 1991). On the contrary,
41
42 717 the Ce concentration in this sample is less depleted, perhaps indicating a key influence of
43
44
45 718 oxygen fugacity in the Ce storage by ophicarbonate minerals.

47 719 The trace element patterns of the majority of the subducted ophicarbonates, and the
48
49
50 720 minerals therein, do not display significant differences from the patterns in the oceanic
51
52 721 samples (**Figs. 5B, D** and **6B, D**). In particular, the coarse and recrystallized calcite in most
53
54 722 deformed subduction-related samples do not show significant differences in their trace
55
56
57 723 element budgets (**Fig. 11A, B** and **C**). This evidence suggests that C-mobilization in these
58
59 724 samples occurred under closed-system conditions. The main differences in composition of the
60
61
62
63
64
65

725 subduction-related ophicarbonates from the oceanic ones are demonstrated by data for the
1 726 eclogitic samples SA15-1 and SA 15-8, which show the highest REE concentrations (note the
2
3 727 enrichment in LREE relative to MREE and HREE in sample SA15-1, **Fig. 5B**) and higher Pb,
4
5 728 As, Sb compared with concentrations in oceanic precursors (**Fig. 5D**). These bulk-rock
6
7 729 anomalies are matched by enrichment in Cs, La, Pb, As, Sb of the rock-forming dolomite and
8
9 730 calcite (**Figs. 6B** and **D**). Enrichment in these elements in ultramafic rocks have been
10
11 731 attributed to exchange with sediment-derived fluids during subduction (Cannaò et al., 2016,
12
13 732 2015; Deschamps et al., 2011; Lafay et al., 2013). Therefore, the bulk-rock and *in-situ* trace
14
15 733 element data suggest that both closed and open system conditions were experienced by
16
17 734 ophicarbonates during the subduction, over their protracted metamorphic histories. In sample
18
19 735 SA 15-8, the vein magnesite traps primary and pseudo-secondary inclusions (**Fig. 3G, H**) of
20
21 736 the fluid that assisted magnesite growth. As expected, the LA-ICP-MS analyses of inclusion-
22
23 737 free and of inclusion-bearing magnesite (**Fig. 11D**) shows that the latter displays much higher
24
25 738 Cs, Ba, B, As, Sb, Rb, W, Pb concentrations. This indicates that the fluid carried crustally-
26
27 739 derived trace elements, either sourced in subducted sedimentary sequences, or released by
28
29 740 dehydration of previously metasomatized altered oceanic crust or associated serpentinites
30
31 741 (e.g., Cannaò and Malaspina, 2018 and reference therein).
32
33
34
35
36
37
38
39
40
41

42 743 *6.3 Tracing C mobility with 3D isotopes*

43
44 744 The oceanic ophicarbonates studied here, like other oceanic ophicarbonates from the
45
46 745 Alps and Pyrenees (e.g., Clerc et al., 2014; Lafay et al., 2017), show wide ranges in O and C
47
48 746 isotope compositions (**Fig. 7A**), depending on the *T* of serpentinization and on the amount of
49
50 747 reduced C contributing to the $\delta^{13}\text{C}$ of the fluids involved (e.g., Alt et al., 2012b; Delacour et
51
52 748 al., 2008). In the oceanic ophicarbonates presented here, the O and C isotope compositions of
53
54 749 calcite are comparable to published values for the Northern Apennine area (Collins et al.,
55
56 750 2015; Galli and Togliatti, 1965; Schwarzenbach et al., 2013). The calcite-seawater isotopic
57
58
59
60
61
62
63
64
65

751 equilibrium indicates that ophicarbonated calcite grew after serpentine over a T range of 130 –
1 752 110 °C (assuming $\delta^{18}\text{O}_{\text{seawater}} = 0\text{‰}$, O’Neil et al., 1969) in OCI and OCII. Lower T of about
2
3 753 110 – 90 °C were obtained for calcite in veins cross-cutting all oceanic structures in OCI and
4
5
6 754 OCII. These T ranges are comparable to those calculated by Schwarzenbach et al. (2013) for
7
8 755 ophicarbonates from the same area (between 150 and 50 °C). All oceanic ophicarbonates
9
10
11 756 presented here preserve a C isotope fingerprint consistent with acquisition of C during
12
13 757 interaction with seawater-derived fluids. In OCII rocks, the matrix calcite in less oxidized
14
15 758 samples (SG 15-4 and SG 15-2) shows slightly lower $\delta^{13}\text{C}$ likely as the result of interaction
16
17
18 759 with serpentinite clasts, showing isotopically negative values (Alt et al., 2012b; Lafay et al.,
19
20 760 2017). The high degree of variability in the C-O isotope compositions of the oceanic protolith
21
22
23 761 has to be taken into account when discussing the evolution of ophicarbonates during
24
25 762 subduction evolution. The $^{87}\text{Sr}/^{86}\text{Sr}$ ratios of the oceanic ophicarbonates investigated here and
26
27
28 763 of the pure serpentinite MNT 15-1 range between 0.7060 and 0.7070 (**Fig. 8**): such values
29
30 764 approach the value of 0.7070 defined for Jurassic seawater (Jones et al., 1994), consistent
31
32
33 765 with carbonation having involved Jurassic seawater re-equilibrated with a mafic/ultramafic
34
35 766 reservoir.

37 767 Carbonate $\delta^{18}\text{O}$ values for the pumpellyite- and of the blueschist-facies ophicarbonates
38
39
40 768 overlap the lower- $\delta^{18}\text{O}$ range for OCI and OCII. The T range achieved for calcite
41
42 769 crystallization in these rocks, based on $\delta^{18}\text{O}$ values, is 130-90 °C (assuming $\delta^{18}\text{O}_{\text{seawater}} = 0\text{‰}$,
43
44
45 770 O’Neil et al., 1969). Such T are in the range for alteration of the oceanic ophicarbonates,
46
47 771 indicating that these ophicarbonates retain the oceanic O isotope imprint of the protolith rocks.
48
49
50 772 Therefore, although subducted ophicarbonates can display either undeformed or deformed
51
52 773 textures attributable to dynamic subduction-zone recrystallization, their $\delta^{18}\text{O}$ does not require
53
54 774 contribution by alteration after seawater-rock interaction. Whereas the O isotope
55
56
57 775 compositions of these rocks are consistent with little or no subduction-related modification of
58
59 776 seafloor compositions, the $\delta^{13}\text{C}$ values (particularly that of sample CU 13-1) could reflect
60
61
62
63
64
65

777 some modification by high-*P* metamorphic fluids. The $\delta^{13}\text{C}$ values of calcite in the
1 778 pumpellyite-facies samples and the undeformed blueschist-facies sample CU3 show no
2
3 779 significant deviation from the values expected for oceanic ophicarbonates (**Fig. 7B**), despite
4
5
6 780 the sampling of two generations of early (coarse) and later (recrystallized) calcite in these
7
8 781 subduction-zone metamorphosed samples (see **Appendix Figure A1**). Coupling this
9
10 782 observation with the preservation of the oceanic $\delta^{18}\text{O}$, with the $^{87}\text{Sr}/^{86}\text{Sr}$ signature (**Fig. 8**),
11
12 783 and the *in-situ* trace element analyses (**Fig. 11A**) indicates inheritance of the oceanic
13
14 784 compositions, at closed-system conditions, during subduction. In contrast, calcite in the
15
16 785 deformed sample CU 13-1 has lower negative $\delta^{13}\text{C}$ values (from -1 to -2‰, **Fig. 7B**) that can
17
18 786 be ascribed to either larger contribution from reduced/organic C during oceanic carbonation
19
20 787 or the influence of reduced C during interaction with fluids sourced during subduction from
21
22 788 the surrounding metasedimentary rocks (Collins et al., 2015; Cook-Kollars et al., 2014). The
23
24 789 more radiogenic Sr isotope composition of CU 13-1 (**Fig. 8**) supports the second scenario (a
25
26 790 metasedimentary source), despite the lack of evidence for significant trace element influx
27
28 791 from sediments based on the *in-situ* analyses (**Fig. 11B**). Carbon additions from
29
30 792 metasedimentary rocks into ultramafic ophicarbonates in the Queyras area has been
31
32 793 documented by means of Fe and Zn isotope systematics by Debret et al. (2018), who showed
33
34 794 that during subduction, these rocks underwent several stages of carbonate dissolution and
35
36 795 precipitation involving sediment-derived fluids.

45 796 One eclogitic sample from the Voltri Massif (LP13 EOC3) affected by ductile
46
47 797 deformation and carbonate recrystallization displays $\delta^{13}\text{C}$ and $\delta^{18}\text{O}$ overlapping values for the
48
49 798 pumpellyite-facies rocks (**Fig. 7B**), suggesting a subduction evolution under closed-system
50
51 799 conditions. This interpretation is supported by a lack of enrichment in FME of the
52
53 800 recrystallized calcite (**Fig. 11C**) and by low radiogenic Sr, with $^{87}\text{Sr}/^{86}\text{Sr}$ still compatible with
54
55 801 an oceanic fingerprint (**Fig. 8**). In contrast, the other eclogitic samples from Voltri Massif are
56
57 802 characterized by the lowest $\delta^{18}\text{O}$ (down to +10.5‰, **Fig. 7B**), matching with the compositions
58
59
60
61
62
63
64
65

803 of the eclogite-facies ophicarbonates from the Zermatt-Saas Zone (Collins et al., 2015),
1 804 whereas their $\delta^{13}\text{C}$ values are similar to those of the other oceanic and subducted
2
3 805 ophicarbonates (**Fig. 7B**). Considering that in these samples, (i) magnesite veins formed
4
5 806 during subduction (sample SA 15-8), (ii) dolomite crystallized together with antigorite and
6
7
8 807 diopside under high- P conditions (sample SA 15-1), and (iii) calcite veins crosscut the
9
10
11 808 prograde antigorite (sample LP13 EOC1), and assuming that their original $\delta^{18}\text{O}$ was the same
12
13 809 as that of the oceanic ophicarbonates, the Voltri ophicarbonates are regarded as having re-
14
15 810 equilibrated with metamorphic fluids that lowered their seafloor-inherited $\delta^{18}\text{O}$ (e.g., Miller
16
17
18 811 and Cartwright, 2000). Decrease in the $\delta^{18}\text{O}$ of these samples is coupled with increase in the
19
20 812 FME budgets of carbonates (**Fig. 6**) and with the bulk-rock enrichment in radiogenic Sr (**Fig.**
21
22 813 **8**), indicating influx of externally-derived fluids.

25 814 Carbonic fluids sourced from metasedimentary rocks during prograde subduction
26
27 815 should be characterized by high $\delta^{18}\text{O}$ and low $\delta^{13}\text{C}$, likely with radiogenic $^{87}\text{Sr}/^{86}\text{Sr}$ reflecting
28
29
30 816 the elevated Rb/Sr of the rocks (Cook-kollars et al., 2014; Yamaguchi et al., 2012). The $\delta^{18}\text{O}$
31
32 817 values of calcite, dolomite and magnesite in the eclogitic ophicarbonates suggest that the
33
34
35 818 fluids in equilibrium with these minerals should have $\delta^{18}\text{O}$ values of +6.7 to +10.5‰ (at peak
36
37 819 T of 500 °C), i.e., +3.8 to +2.5‰ lower than the associated minerals (using the $\Delta^{18}\text{O}_{\text{carbonate-}}$
38
39
40 820 water of Zheng, 1999). Such isotopic values are compatible with derivation of the fluids from
41
42 821 altered oceanic crust and/or serpentinitized mantle (Cartwright and Barnicoat, 1999) rather than
43
44
45 822 sedimentary sources (see Jaekel et al., 2018). However, the Sr isotope ratios of oceanic,
46
47 823 mafic crustal reservoirs are generally less radiogenic than values for the ophicarbonates
48
49
50 824 analyzed in this study. The conundrum is possibly solved by associating the isotopic imprints
51
52 825 observed in the high- P ophicarbonates with interaction with fluids released by devolatilization
53
54 826 of hybridized ultramafic rocks bearing some sedimentary signatures. As a related example,
55
56
57 827 Cannà et al. (2016) demonstrated that interaction of sediment-derived fluids with the Voltri
58
59 828 serpentinites caused enrichments in FME and provided radiogenic Sr and Pb. The subduction
60
61
62
63
64
65

829 dehydration of such a hybrid serpentinite could have released hydrous fluids contributing the
1 830 isotopic signatures to the subduction ophiocarbonates analyzed in this study (high $^{87}\text{Sr}/^{86}\text{Sr}$,
2
3 831 low $\delta^{18}\text{O}$, FME enrichment). Beginning with serpentinites with + 6 / +8‰ $\delta^{18}\text{O}$ (Cannaò et al.,
4
5 832 2016; Früh-Green et al., 2001), the fluids released at 400 to 650 °C, corresponding to the
6
7 833 temperatures of olivine-in and antigorite-out reactions (Scambelluri et al., 1995), would have
8
9 834 $\delta^{18}\text{O}$ ranging from +7.2 to +10.8‰. These values are in good agreement with those of the
10
11 835 metamorphic fluids in equilibrium with carbonates from the subduction-zone ophiocarbonates
12
13 836 for which data are presented in this paper. The fluid generated by devolatilization of the
14
15 837 serpentinite also would have low C/O ratio (Alt et al., 2012a), enabling retention of the C
16
17 838 isotope compositions of the carbonates, even at fairly high fluid-rock ratios, but modifying the
18
19 839 $\delta^{18}\text{O}$ towards lower values. Alternatively, interaction of fluids derived by de-serpentinization
20
21 840 with metasedimentary rocks along their flow paths in the subduction zone, could have led to
22
23 841 the hybridized fluid compositions. Other recent studies of extensively veined mafic rocks and
24
25 842 Schistes Lustrés adjacent to fault systems though to represent transient subduction interfaces
26
27 843 has demonstrated shifts in $\delta^{18}\text{O}$ to similar values and invoked infiltration by H₂O-rich fluids
28
29 844 generated by dehydration of mafic and/or ultramafic rocks at greater depths (Angiboust et al.,
30
31 845 2017; Epstein et al., 2019; Jaeckel et al., 2018).
32
33
34
35
36
37
38
39
40
41

42 847 7. Conclusions

43
44 848 In this study, we provide petrographic and geochemical constraints regarding fluid-
45
46 849 driven C mobility in ophiocarbonates representing shallow levels of subduction zones and their
47
48 850 equivalents subducted to depths experiencing eclogitic *P-T* conditions. We characterize the
49
50 851 sources of these fluids, identifying cases where compositions can be explained by closed-
51
52 852 system conditions and others where open-system fluid-rock interaction appears to have been
53
54 853 required. We demonstrate that decarbonation and dissolution/precipitation processes
55
56 854 operating in ancient subduction zones are best traced using a combination of detailed field and
57
58
59
60
61
62
63
64
65

855 petrographic observations, FME inventories and C-O and Sr isotope systematics. We suggest
1 856 that one challenge to our better understanding subduction zone C fluxes is the upscaling of
2
3 857 observations from field and geochemical studies of high-*P* metamorphic rocks to
4
5
6 858 consideration of C cycling at Earth's modern consuming margins.
7

8 859
9

10 860 **Acknowledgements**

13 861 EC acknowledges funding by the Italian Society of Mineralogy and Petrology (SIMP
14
15 862 award "Borsa di Studio per l'estero 2015") for supporting his visit to Lehigh University, and
16
17
18 863 the CNR for providing a Short-Term Mobility grant to visit the Bern University for in-situ
19
20 864 analyses. During the preparation of the manuscript EC was supported by the Italian MIUR
21
22
23 865 PRIN project 2015C5LN35. The project has been supported by funds of the University of
24
25 866 Genova and of the Italian MIUR to MS (MIUR PRIN projects 2012R33ECR_002 and
26
27
28 867 2017ZE49E7), of the USA-National Science Foundation to GEB (grant EAR-1119264) and
29
30 868 of the IGG-CNR-P0000514 to SA. Constructive reviews by J. Alt and anonymous reviewer,
31
32
33 869 and manuscript handling by Editor C. Chauvel, greatly improved the presentation of the
34
35 870 manuscript and have been much appreciated.
36

37 871
38
39

40 872 **Figure Caption**

42 873 **Figure 1**

45 874 Simplified geological map of the Western Alps and location of the studied areas (modify after
46
47 875 Collins et al., 2015). (A) Geological map of Internal Liguride from the Ligurian N. Apennine
48
49 876 ophiolite (modified after Treves and Harper, 1994); (B) area of study from the Queyras/Ubaye
50
51
52 877 zone (modified after Michard et al., 2004); (C) geological map of the Voltri Massif (modified
53
54 878 after Cannà et al., 2016 and reference therein). Locations of the collected samples for all
55
56
57 879 three areas of study together with the respective sample' labels are indicated with the star
58
59 880 symbol.
60
61
62
63
64
65

1 882 **Figure 2**

2
3 883 Photomicrographs of the tectonic/hydrothermal (OCI) and sedimentary (OCII) ophicarbonates
4
5
6 884 from the Northern Apennines: (A) parallel and (B) crossed polarized light microphotographs
7
8 885 of completely carbonated serpentinite clast. Equant calcite grains overgrowing
9
10
11 886 pseudomorphic serpentine minerals in the cell of mesh texture and a film of hematite grown
12
13 887 along the border, giving them a ghost-like texture (OCI – MNT 13-5). (C) Former
14
15 888 porphyroclast of serpentinitized pyroxene (i.e., bastite; red dashed line) partially carbonated
16
17
18 889 coupled with formation of oceanic garnet along the cleavage (OCI – ISC 13-1). (D) Talc
19
20 890 aggregates overgrowing coarse grains of calcite in tardive veins. This represents the last
21
22
23 891 process affecting the oceanic ophicarbonates (OCI – MNT 13-5). (E) Boytroidal versus
24
25 892 irregular blocky calcite in vein (OCII – SG15-4). (F) Calcite in sedimentary matrix rich in
26
27
28 893 hematite. Several serpentinite (Serp) clasts with irregular shape are visible (OCII – MNT 15-
29
30 894 2).

31
32 89533
34
35 896 **Figure 3**

36
37 897 Photomicrographs of the subducted ophicarbonates. (A) Old elongated and strained calcite
38
39
40 898 grains, partially recrystallized along grain boundaries. Complete recrystallization of un-
41
42 899 twinned calcites along major shear zone is visible (PL 13-2). (B) Re-oriented serpentinite
43
44
45 900 clast along the shear zone partially carbonated (Carb clast). Relict of twinned calcites are
46
47 901 visible enclosed in recrystallized prograde calcite mylonites (PL 13-2). (C) Stretched
48
49
50 902 serpentinite clast (Serp) with microfractures and pressure shadows filled by syn-tectonic
51
52 903 extensional calcite-fibers (Syn-tect. calcite). Syn-tectonic calcite is probably linked to the
53
54 904 oceanic stage (CU3). (D) Dynamic recrystallization of old strained calcite porphyroclasts
55
56
57 905 producing fine untwinned calcite grains (CU 13-1). (E) Green garnet (Andradite) associated
58
59 906 with oxide (Cr-magnetite – Cr-mgt) and calcite along major deformation zone (LP13 EOC1).
60
61
62
63
64
65

907 (F) Relict of the high pressure layer with dolomite + diopside + antigorite (SA 15-1). (G-H)

1 908 Primary and pseudo-secondary fluid inclusions (FI) hosted in magnesite (Mgs) from sample

2

3 909 SA 15-8.

4

5 910

6

7 911 **Figure 4**

8

9 912 Bulk-rock major element data showing the relationship between CaO, MgO and SiO₂ of

10

11 913 ophicarbonates as well as variations in CO₂ and H₂O with respect to MgO and CaO.

12

13 914 Oceanic and subducted ophicarbonates fall in between pure serpentinite and limestone end-

14

15 915 members.

16

17 916

18

19 917 **Figure 5**

20

21 918 Primitive mantle normalized (McDonough and Sun, 1995) Rare Earth Element (REE) and

22

23 919 trace element patterns of ophicarbonates from oceanic (A, C) and subduction (B, D) stages. In

24

25 920 (A) the grey field report the range of the peridotites from Internal Liguride (Rampone et al.,

26

27 921 1996). In (B) and (D), the grey fields represent the REE and trace element pattern of the

28

29 922 oceanic oph carbonate illustrated in (A) and (C).

30

31 923

32

33 924 **Figure 6**

34

35 925 Primitive mantle normalized trace elements patterns of serpentine and carbonate from oceanic

36

37 926 (A, C) and subduction (B, D) stages. In (B) and (D) grey fields represent the trace element

38

39 927 variation of the serpentine and calcite from oceanic origin illustrated in (A) and (C). Primitive

40

41 928 mantle normalization from McDonough and Sun (1995).

42

43 929

44

45 930 **Figure 7**

46

47 931 Oxygen ($\delta^{18}\text{O}_{\text{VSMOW}}$) and C ($\delta^{13}\text{C}_{\text{VPDB}}$) isotopic signatures of ophicarbonates from oceanic

48

49 932 (A) and subduction (B) stages. In (A) oph carbonate fields from Bracco, the Pyrenean and

50

51

52

53

54

55

56

933 Chenaillet (with different grey colours) are shown for comparison (from Collins et al., 2015;
1 934 Clerc et al., 2014; Lafay et al., 2017). In **(B)** the Queyras and Zermatt-Saas fields are from
2
3 935 Collins et al., (2015) whereas Chatillon ophicarbonates field is from Driesner (1993). The
4
5
6 936 complete $\delta^{18}\text{O}$ vs. $\delta^{13}\text{C}$ dataset is shown in the **Appendix Figure A1** and in the
7
8 937 **Supplementary Table S2.**

9
10 938

13 939 **Figure 8**

14
15 940 $^{87}\text{Sr}/^{86}\text{Sr}$ vs. $\delta^{18}\text{O}_{\text{VSMOW}}$ **(A)** and $\delta^{13}\text{C}_{\text{VPDB}}$ **(B)** of ophicarbonates studied in this work. For
16
17
18 941 comparison the values of the pure oceanic serpentinite and limestone from the Northern
19
20 942 Apennines and of the Jurassic seawater are shown (dashed black lines).

21
22
23 943

25 944 **Figure 9**

26
27 945 Cartoon illustrating the sequence of hydration and carbonation/oxidation processes affecting
28
29
30 946 mantle rocks at oceanic conditions. See text for discussion.

31
32
33 947

35 948 **Figure 10**

36
37 949 Activity-activity diagram for Si and CO_2 ($\log(a\text{SiO}_2)$ and $\log(a\text{CO}_2)$, respectively) depicting
38
39
40 950 phase equilibria in the $\text{MgO-CaO-Al}_2\text{O}_3\text{-SiO}_2\text{-H}_2\text{O-CO}_2$ system at 100 °C and 1500 bar
41
42 951 (calculated using the *Perple_X* software, Connolly (2005) and the internal consistent
43
44
45 952 thermodynamic database of Holland and Powell (1998) and the compensated Redlich-Kwong
46
47 953 (CORK) equation of state of Holland and Powell (1991) for H_2O and CO_2 fluids). Key
48
49 954 carbonate-in (in red), talc-in (in green) and release H_2O (in blue) boundaries are emphasized.
50
51
52 955 See text for discussion.

53
54 956

57 957 **Figure 11**

58
59
60
61
62
63
64
65

958 Comparison between in situ trace elements data for coarse and recrystallized calcite from
1 959 pumpellyite- (A), blueschist- (B) and eclogite-facies (C) samples. Trace element
2
3 960 compositions of fluid inclusion – magnesite mixed measurement compared with pure
4
5
6 961 magnesite are reported in (D). Primitive mantle data from McDonough and Sun (1995).
7

8 962
9

10 963 **References**

11
12
13 964 Agard, P., Jolivet, L., Goffé, B., 2001. Tectonometamorphic evolution of the Schistes Lustres
14
15 965 Complex; implications for the exhumation of HP and UHP rocks in the Western Alps.

16
17
18 966 Bull. la Soc. Geol. Fr. <https://doi.org/10.2113/172.5.617>

19
20 967 Ague, J.J., Nicolescu, S., 2014. Carbon dioxide released from subduction zones by fluid-
21
22 968 mediated reactions. *Nat. Geosci.* 7, 355–360. <https://doi.org/10.1038/ngeo2143>

23
24
25 969 Allen, D.E., Seyfried, W.E., 2005. REE controls in ultramafic hosted MOR hydrothermal
26
27 970 systems: an experimental study at elevated temperature and pressure. *Geochim.*

28
29
30 971 *Cosmochim. Acta* 69, 675–683.

31
32 972 Alt, J.C., Crispini, L., Gaggero, L., Levine, D., Lavagnino, G., Shanks, P., Gulbransen, C.,
33
34
35 973 2018. Normal faulting and evolution of fluid discharge in a Jurassic seafloor ultramafic-
36
37 974 hosted hydrothermal system. *Geology* 46, 523–526. <https://doi.org/10.1130/G40287.1>

38
39
40 975 Alt, J.C., Garrido, C.J., Shanks, W.C.C., Turchyn, A., Padrón-Navarta, J.A., López Sánchez-
41
42 976 Vizcaíno, V., Gómez Pugnare, M.T., Marchesi, C., Sánchez-Vizcaíno, V.L., Pugnare,
43
44
45 977 M.T.G., 2012a. Recycling of water, carbon, and sulfur during subduction of
46
47 978 serpentinites: A stable isotope study of Cerro del Almiraz, Spain. *Earth Planet. Sci. Lett.*
48
49 979 327, 50–60. <https://doi.org/10.1016/j.epsl.2012.01.029>

50
51
52 980 Alt, J.C., Schwarzenbach, E.M., Früh-Green, G.L., Shanks, W.C., Bernasconi, S.M., Garrido,
53
54 981 C.J., Crispini, L., Gaggero, L., Padrón-Navarta, J.A., Marchesi, C., 2013. The role of
55
56
57 982 serpentinites in cycling of carbon and sulfur: Seafloor serpentinization and subduction
58
59 983 metamorphism. *Lithos* 178, 40–54. <https://doi.org/10.1016/j.lithos.2012.12.006>
60
61
62
63
64
65

- 984 Alt, J.C., Shanks, W.C.C., Crispini, L., Gaggero, L., Schwarzenbach, E.M., Früh-Green, G.L.,
1 985 Bernasconi, S.M., 2012b. Uptake of carbon and sulfur during seafloor serpentinization
2
3 986 and the effects of subduction metamorphism in Ligurian peridotites. *Chem. Geol.* 322–
4
5 987 323, 268–277. <https://doi.org/10.1016/j.chemgeo.2012.07.009>
7
8 988 Andreani, M., Escartin, J., Delacour, A., Ildefonse, B., Godard, M., Dyment, J., Fallick, A.E.,
9
10 989 Fouquet, Y., 2014. Tectonic structure, lithology, and hydrothermal signature of the
11
12 990 rainbow massif (Mid-Atlantic Ridge 36° 14'N). *Geochemistry, Geophys. Geosystems.*
13
14 991 <https://doi.org/10.1002/2014GC005269>
15
16 992 Angiboust, S., Yamato, P., Hertgen, S., Hyppolito, T., Bebout, G.E., Morales, L., 2017. Fluid
17
18 993 pathways and high-P metasomatism in a subducted continental slice (Mt. Emilius klippe,
19
20 994 W. Alps). *J. Metamorph. Geol.* 35, 471–492. <https://doi.org/10.1111/jmg.12241>
21
22 995 Bailey, E.H., Ragnarsdottir, K. V., 1994. Uranium and Thorium Solubilities in Subduction
23
24 996 Zone (Vol 124, Pg 119, 1994). *Earth Planet. Sci. Lett.* 128, 705–706.
25
26 997 Barbieri, M., Masi, U., Tolomeo, L., 1979. Stable isotope evidence for a marine origin of
27
28 998 ophicalcites from the north-central Apennines (Italy). *Mar. Geol.* 30, 193–204.
29
30 999 [https://doi.org/10.1016/0025-3227\(79\)90015-X](https://doi.org/10.1016/0025-3227(79)90015-X)
31
32 1000 Berner, R.A., 1998. The carbon cycle and CO₂ over Phanerozoic time: The role of land plants.
33
34 1001 *Philos. Trans. R. Soc. B Biol. Sci.* 353, 75–82. <https://doi.org/10.1098/rstb.1998.0192>
35
36 1002 Bonatti, E., 1976. Serpentinite protrusions in the oceanic crust. *Earth Planet. Sci. Lett.* 32,
37
38 1003 107–113.
39
40 1004 Caciagli, N.C., Manning, C.E., 2003. The solubility of calcite in water at 6-16 kbar and 500-
41
42 1005 800 °C. *Contrib. to Mineral. Petrol.* 146, 275–285. [https://doi.org/10.1007/s00410-003-](https://doi.org/10.1007/s00410-003-0501-y)
43
44 1006 0501-y
45
46 1007 Cannà, E., Agostini, S., Scambelluri, M., Tonarini, S., Godard, M., 2015. B, Sr and Pb
47
48 1008 isotope geochemistry of high-pressure Alpine metaperidotites monitors fluid-mediated
49
50 1009 element recycling during serpentinite dehydration in subduction mélange (Cima di
51
52
53
54
55
56
57
58
59
60
61
62
63
64
65

- 1010 Gagnone, Swiss Central Alps). *Geochim. Cosmochim. Acta* 163, 80–100.
- 1011 <https://doi.org/10.1016/j.gca.2015.04.024>
- 1012 Cannà, E., Malaspina, N., 2018. From oceanic to continental subduction : Implications for
1013 the geochemical and redox evolution of the supra-subduction mantle 14.
- 1014 <https://doi.org/10.1130/GES01597.1/4457636/ges01597.pdf>
- 1015 Cannà, E., Scambelluri, M., Agostini, S., Tonarini, S., Godard, M., 2016. Linking
1016 serpentinite geochemistry with tectonic evolution at the subduction plate-interface: The
1017 Voltri Massif case study (Ligurian Western Alps, Italy). *Geochim. Cosmochim. Acta*
1018 190, 115–133. <https://doi.org/10.1016/j.gca.2016.06.034>
- 1019 Carpena, J., Caby, R., 1984. Fission-track evidence for Late Triassic oceanic crust in the
1020 French Occidental Alps. *Geology*. [https://doi.org/10.1130/0091-
1021 7613\(1984\)12<108:FEFLTO>2.0.CO;2](https://doi.org/10.1130/0091-7613(1984)12<108:FEFLTO>2.0.CO;2)
- 1022 Cartwright, I., Barnicoat, A.C., 1999. Stable isotope geochemistry of Alpine ophiolites: A
1023 window to ocean-floor hydrothermal alteration and constraints on fluid-rock interaction
1024 during high-pressure metamorphism. *Int. J. Earth Sci.* 88, 219–235.
- 1025 <https://doi.org/10.1007/s005310050261>
- 1026 Chiesa, S., Cortesogno, L., Forcella, F., Galli, M., Messiga, B., Pasquaré, G., Pedemonte,
1027 G.M., Piccardo, G.B., Rossi, P.M., 1975. Assetto strutturale ed interpretazione
1028 geodinamica del Gruppo di Voltri. *Boll. Soc. Geol. Ital.* 94, 555–581.
- 1029 Cimmino, F., Messiga, B., Piccardo, G.B., Zeda, O., 1979. Titanian clinohumite-bearing
1030 assemblages within antigoritic serpentinites of the Voltri Massif (Western Liguria):
1031 interferences on the geodynaminc evolution of piemontese ultramafic sections. *Ofioliti* 4,
1032 97–120.
- 1033 Clerc, C., Boulvais, P., Lagabrielle, Y., Blanquat, M.D. Saint, 2014. Opicalcites from the
1034 northern Pyrenean belt : a field , petrographic and stable isotope study 141–163.
- 1035 <https://doi.org/10.1007/s00531-013-0927-z>

- 1036 Collins, N.C., Bebout, G.E., Angiboust, S., Agard, P., Scambelluri, M., Crispini, L., John, T.,
1037 2015. Subduction zone metamorphic pathway for deep carbon cycling : II . Evidence
1038 from HP / UHP metabasaltic rocks and ophiocarbonates. *Chem. Geol.* 412, 132–150.
1039 <https://doi.org/10.1016/j.chemgeo.2015.06.012>
- 1040 Connolly, J.A.D., 2005. Computation of phase equilibria by linear programming : A tool for
1041 geodynamic modeling and its application to subduction zone decarbonation 236, 524–
1042 541. <https://doi.org/10.1016/j.epsl.2005.04.033>
- 1043 Cook-Kollars, J., Bebout, G.E., Collins, N.C., Angiboust, S., Agard, P., 2014. Subduction
1044 zone metamorphic pathway for deep carbon cycling: I. Evidence from HP/UHP
1045 metasedimentary rocks, Italian Alps. *Chem. Geol.* 386, 31–48.
1046 <https://doi.org/10.1016/j.chemgeo.2014.07.013>
- 1047 Cortesogno, L., Galbiati, B., Principi, G., 1980. Le breccie serpentinitiche giurassiche della
1048 Liguria orientale. *Arch. Sci. Genève* 33, 185–200.
- 1049 Cortesogno, L., Lucchetti, G., Massa, B., 1981. Rocce ofi-carbonate e marmi a silicati nel
1050 Massiccio di Voltri: origine e significato, chimismo dei minerali ed equilibri paragenetici.
1051 *Rend. Soc. Ital. di Mineral. e Petrol.* 37, 481–507.
- 1052 Crispini, L., Capponi, G., 2001. Tectonic evolution of the Voltri Group and Sestri Voltaggio
1053 Zone (southern limit of the NW Alps): a review. *Ophioliti* 26, 161–164.
- 1054 Dasgupta, R., Hirschmann, M.M., 2010. The deep carbon cycle and melting in Earth ' s
1055 interior. *Earth Planet. Sci. Lett.* 298, 1–13. <https://doi.org/10.1016/j.epsl.2010.06.039>
- 1056 Debret, B., Bouilhol, P., Pons, M.L., Williams, H., 2018. Carbonate transfer during the onset
1057 of slab devolatilization: New insights from Fe and Zn stable isotopes. *J. Petrol.* 59, 1145–
1058 1166. <https://doi.org/10.1093/petrology/egy057>
- 1059 Decandia, F.A., Lazzarotto, A., Liotta, D., Cernobori, L., Nicolich, R., 1998. The CROP3
1060 traverse: insights on post-collisional evolution of Northern Apennines.
- 1061 Delacour, A., Früh-Green, G.L., Frank, M., Gutjahr, M., Kelley, D.S., 2008. Sr-and Nd-

- 1062 isotope geochemistry of the Atlantis Massif (30 N, MAR): implications for fluid fluxes
1063 and lithospheric heterogeneity. *Chem. Geol.* 254, 19–35.
- 1064 Deschamps, F., Godard, M., Guillot, S., Hattori, K., 2013. Geochemistry of subduction zone
1065 serpentinites: A review. *Lithos* 178, 96–127. <https://doi.org/10.1016/j.lithos.2013.05.019>
- 1066 Deschamps, F., Guillot, S., Godard, M., Andreani, M., Hattori, K., 2011. Serpentinites act as
1067 sponges for fluid-mobile elements in abyssal and subduction zone environments. *Terra*
1068 *Nov.* 23, 171–178.
- 1069 Driesner, T., 1993. Aspects of Petrographic, Structural and Stable Isotope Geochemical
1070 Evolution of Ophicarbonates Breccias from Ocean-Floor to Subduction and Uplift - an
1071 Example from Chatillon, Middle Aosta Valley, Italian Alps. *Schweizerische Mineral.*
1072 *Und Petrogr. Mitteilungen* 73, 69–84.
- 1073 Epstein, G., Angiboust, S., Bebout, G., 2019. Scales of Fluid-Rock Interaction and Carbon
1074 Mobility in the Deeply Underplated and HP -Metamorphosed Schistes Lustrés , Western
1075 Alps. *LITHOS* 105229. <https://doi.org/10.1016/j.lithos.2019.105229>
- 1076 Federico, L., Capponi, G., Crispini, L., Scambelluri, M., 2004. Exhumation of alpine high-
1077 pressure rocks: Insights from petrology of eclogite clasts in the Tertiary Piedmontese
1078 basin (Ligurian Alps, Italy). *Lithos* 74, 21–40.
<https://doi.org/10.1016/j.lithos.2003.12.001>
- 1079 Federico, L., Crispini, L., Scambelluri, M., Capponi, G., 2007. Ophiolite melange zone
1080 records exhumation in a fossil subduction channel. *Geology* 35, 499–502.
<https://doi.org/10.1130/G23190A.1>
- 1083 Frezzotti, M.L., Selverstone, J., Sharp, Z.D., Compagnoni, R., 2011. Carbonate dissolution
1084 during subduction revealed by diamond-bearing rocks from the Alps. *Nat. Geosci.* 4,
1085 703–706. <https://doi.org/10.1038/ngeo1246>
- 1086 Früh-Green, G.L., Connolly, J.A.D., Plas, A., Kelley, D.S., Grobety, B., 2004.
1087 Serpentinization of Oceanic Peridotites : Implications for Geochemical Cycles and

- 1088 Biological Activity The Subseafloor Biosphere at Mid-Ocean Ridges. *Geophys. Monogr.*
1089 Ser. 144, 119–136.
- 1090 Früh-Green, G.L., Scambelluri, M., Vallis, F., 2001. O-H isotope ratios of high pressure
1091 ultramafic rocks: Implications for fluid sources and mobility in the subducted hydrous
1092 mantle. *Contrib. to Mineral. Petrol.* 141, 145–159.
1093 <https://doi.org/10.1007/s004100000228>
- 1094 Früh-Green, G.L., Weissert, H., Bernoulli, D., 1990. A multiple fluid history recorded in
1095 Alpine ophiolites. *J. Geol. Soc. London.* 147, 959–970.
1096 <https://doi.org/10.1144/gsjgs.147.6.0959>
- 1097 Galli, M., 1957. Il Rosso di Levanto. *Rend. Soc. Miner. Ital* 13, 265–267.
- 1098 Galli, M., Togliatti, V., 1965. Ricerche petrografiche sulla formazione ofiolitica
1099 dell'Appennino Ligure. Il Rosso di Levanto—nuovo contributo. *Ann. Mus. Civ. St. Nat.*
1100 Genova 75, 359–381.
- 1101 Godard, M., Joussetin, D., Bodinier, J.-L., 2000. Relationships between geochemistry and
1102 structure beneath a palaeo-spreading centre: a study of the mantle section in the Oman
1103 ophiolite. *Earth Planet. Sci. Lett.* 180, 133–148.
- 1104 Grozeva, N.G., Klein, F., Seewald, J.S., Sylva, S.P., 2017. Experimental study of carbonate
1105 formation in oceanic peridotite. *Geochim. Cosmochim. Acta* 199, 264–286.
1106 <https://doi.org/10.1016/j.gca.2016.10.052>
- 1107 Guillong, M., Meier, D.L., Allan, M.M., Heinrich, C.A., Yardley, B.W.D., 2008. Appendix
1108 A6: SILLS: a MATLAB-based program for the reduction of laser ablation ICP-MS data
1109 of homogeneous materials and inclusions 328–333.
- 1110 Halter, W.E., Pettke, T., Heinrich, C.A., Rothen-Rutishauser, B., 2002. Major to trace element
1111 analysis of melt inclusions by laser-ablation ICP-MS: Methods of quantification. *Chem.*
1112 *Geol.* 183, 63–86. [https://doi.org/10.1016/S0009-2541\(01\)00372-2](https://doi.org/10.1016/S0009-2541(01)00372-2)
- 1113 Harvey, J., Garrido, C.J., Savov, I.P., Agostini, S., Padrón-Navarta, J.A., Marchesi, C.,

- 1114 Sánchez-Vizcaíno, V.L., Gómez-Pugnaire, M.T., 2014. 11 B-rich fluids in subduction
1115 zones: The role of antigorite dehydration in subducting slabs and boron isotope
1116 heterogeneity in the mantle. *Chem. Geol.* 376, 20–30.
- 1117 Hermann, J., Müntener, O., Scambelluri, M., Mu, O., 2000. The importance of serpentinite
1118 mylonites for subduction and exhumation of oceanic crust. *Tectonophysics* 327, 225–
1119 238. [https://doi.org/10.1016/S0040-1951\(00\)00171-2](https://doi.org/10.1016/S0040-1951(00)00171-2)
- 1120 Holland, T., Powell, R., 1991. A Compensated-Redlich-Kwong (CORK) equation for
1121 volumes and fugacities of CO₂ and H₂O in the range 1 bar to 50 kbar and 100-1600°C.
1122 *Contrib. to Mineral. Petrol.* <https://doi.org/10.1007/BF00306484>
- 1123 Holland, T.J.B., Powell, R., 1998. An internally consistent thermodynamic data set for phases
1124 of petrological interest. *J. Metamorph. Geol.* 16, 309–343.
1125 <https://doi.org/10.1111/j.1525-1314.1998.00140.x>
- 1126 Hoogerduijn Strating, E.H., Rampone, E., Piccardo, G.B., Drury, M.R., Vissers, R.L.M., 1993.
1127 Subsolidus emplacement of mantle peridotites during incipient oceanic rifting and
1128 opening of the Mesozoic Tethys (Voltri Massif, NW Italy). *J. Petrol.* 34, 901–927.
- 1129 Ionov, D.A., Savoyant, L., Dupuy, C., 1992. Application of the ICP-MS technique to trace
1130 element analysis of peridotite and their minerals. *Geostand. Newsl.* 16, 311–315.
- 1131 Jaeckel, K., Bebout, G.E., Angiboust, S., 2018. Deformation-enhanced fluid and mass transfer
1132 along Western and Central Alps paleo-subduction interfaces: Significance for carbon
1133 cycling models. *Geosphere* 14, 2355–2375. <https://doi.org/10.1130/GES01587.1>
- 1134 Jochum, K.P., Nohl, U., Herwig, K., Lammel, E., Stoll, B., Hofmann, A.W., 2005. GeoReM:
1135 A New Geochemical Database for Reference Materials and Isotopic Standards. *Geostand.*
1136 *Geoanalytical Res.* 29, 333–338. <https://doi.org/10.1111/j.1751-908x.2005.tb00904.x>
- 1137 Jones, C.E., Jenkyns, H.C., Coe, A.L., Stephen, H.P., 1994. Strontium isotopic variations in
1138 Jurassic and Cretaceous seawater. *Geochim. Cosmochim. Acta* 58, 3061–3074.
- 1139 Kelemen, P.B., Manning, C.E., 2015. Reevaluating carbon fluxes in subduction zones, what

- 1140 goes down, mostly comes up. Proc. Natl. Acad. Sci. 112, E3997–E4006.
- 1141 <https://doi.org/10.1073/pnas.1507889112>
- 1142 Kelley, D.S., Karson, J.A., Fru, G.L., Yoerger, D.R., Shank, T.M., Butterfield, D.A., Hayes,
1143 J.M., Schrenk, M.O., Olson, E.J., Proskurowski, G., Jakuba, M., Bradley, A., Larson, B.,
1144 Ludwig, K., Glickson, D., Buckman, K., Bradley, A.S., Brazelton, W.J., Roe, K.,
1145 Bernasconi, S.M., Elend, M.J., Lilley, M.D., Baross, J.A., Summons, R.E., Sylva, S.P.,
1146 2005. Kelley_05 307, 1–7.
- 1147 Keppler, H., Wyllie, P.J., 1991. Partitioning of Cu, Sn, Mo, W, U, and Th between melt and
1148 aqueous fluid in the systems haplogranite-H₂O-HCl and haplogranite-H₂O-HF. Contrib.
1149 to Mineral. Petrol. <https://doi.org/10.1007/BF00306474>
- 1150 Kerrick, D.M., Connolly, J.A.D., 2001. Metamorphic devolatilization of subducted marine
1151 sediments and the transport of volatiles into the Earth ' s mantle 36, 293–296.
- 1152 Kerrick, D.M., Connolly, J.A.D., 1998. Subduction of ophiicarbonates and recycling of CO₂
1153 and H₂O. Geology 26, 375–378.
- 1154 Klein, F., Garrido, C.J., 2011. Thermodynamic constraints on mineral carbonation of
1155 serpentinized peridotite. Lithos 126, 147–160.
1156 <https://doi.org/10.1016/j.lithos.2011.07.020>
- 1157 Kodolányi, J., Pettke, T., Spandler, C., Kamber, B.S., Ling, K.G., Gme, K., 2012.
1158 Geochemistry of ocean floor and fore-arc serpentinites: Constraints on the ultramafic
1159 input to subduction zones. J. Petrol. 53, 235–270.
1160 <https://doi.org/10.1093/petrology/egr058>
- 1161 Lafay, R., Baumgartner, L.P., Stephane, S., Suzanne, P., German, M.H., Torsten, V., 2017.
1162 Petrologic and stable isotopic studies of a fossil hydrothermal system in ultramafic
1163 environment (Chenaillet ophiolites, Western Alps, France): Processes of carbonate
1164 cementation. Lithos 294–295, 319–338. <https://doi.org/10.1016/j.lithos.2017.10.006>
- 1165 Lafay, R., Deschamps, F., Schwartz, S., Guillot, S., Godard, M., Debret, B., Nicollet, C., 2013.

- 1166 High-pressure serpentinites, a trap-and-release system controlled by metamorphic
1167 conditions: Example from the Piedmont zone of the western Alps. *Chem. Geol.* 343, 38–
2 54.
3 1168
4
5
6 1169 Lafay, R., Montes-Hernandez, G., Janots, E., Munoz, M., Auzende, A.L., Gehin, A., Chiriach,
7
8 1170 R., Proux, O., 2016. Experimental investigation of As, Sb and Cs behavior during olivine
9
10 serpentinitization in hydrothermal alkaline systems. *Geochim. Cosmochim. Acta* 179,
11 177–202. <https://doi.org/10.1016/j.gca.2016.02.014>
12
13 1172
14
15 1173 Lagabrielle, Y., 1987. Les ophiolites: marqueurs de l'histoire tectonique des domaines
16
17 océaniques: le cas des Alpes franco-italiennes (Queyras, Piémont). Brest.
18 1174
19
20 1175 Lagabrielle, Y., Lemoine, M., Tricart, P., 1985. Paléotectonique océanique et déformations
21
22 alpines dans le massif ophiolitique du Pelvas d'Abriès (Alpes Occidentales-Queyras-
23 1176 France). *Bull. la Société Géologique Fr.* 1, 473–480.
24
25 1177
26
27 1178 Lemoine, M., Tricart, P., Boillot, G., 1987. Ultramafic and gabbroic ocean floor of the
28
29 Ligurian Tethys (Alps, Corsica, Apennines): in search of a genetic model. *Geology* 15,
30 622–625. [https://doi.org/10.1130/0091-7613\(1987\)15<622:UAGOFO>2.0.CO;2](https://doi.org/10.1130/0091-7613(1987)15<622:UAGOFO>2.0.CO;2)
31
32 1180
33
34
35 1181 Leoni, L., Marroni, M., Sartori, F., Tamponi, M., 1996. Metamorphic grade in metapelites of
36
37 the Internal Liguride Units (Northern Apennines, Italy). *Eur. J. Mineral.* 8, 70176.
38
39
40 1183 <https://doi.org/10.1127/ejm/8/1/0035>
41
42 1184 Ludwig, K.A., Kelley, D.S., Butterfield, D.A., Nelson, B.K., Früh-Green, G.L., 2006.
43
44 Formation and evolution of carbonate chimneys at the Lost City Hydrothermal Field.
45 1185
46
47 1186 *Geochim. Cosmochim. Acta* 70, 3625–3645. <https://doi.org/10.1016/j.gca.2006.04.016>
48
49
50 1187 Malaspina, N., Poli, S., Fumagalli, P., 2009. The oxidation state of metasomatized mantle
51
52 wedge: Insights from C-O-H-bearing garnet peridotite. *J. Petrol.* 50, 1533–1552.
53
54 1189 <https://doi.org/10.1093/petrology/egp040>
55
56
57 1190 Malatesta, C., Crispini, L., Federico, L., Capponi, G., Scambelluri, M., 2012. The exhumation
58
59 of high pressure ophiolites (Voltri Massif, Western Alps): Insights from structural and
60
61
62
63
64
65

- 1192 petrologic data on metagabbro bodies. *Tectonophysics* 568–569, 102–123.
1193 <https://doi.org/10.1016/j.tecto.2011.08.024>
- 1194 McCrea, J.M., 1950. On the isotopic chemistry of carbonates and a paleotemperature scale. *J.*
1195 *Chem. Phys.* <https://doi.org/10.1063/1.1747785>
- 1196 McDonough, W.F., Sun, S.-S., 1995. The composition of the Earth. *Chem. Geol.* 120, 223–
1197 253.
- 1198 Messiga, B., Scambelluri, M., 1991. Retrograde P-T-T path for the Voltri-Massif eclogites
1199 (Ligurian Alps, Italy) - some tectonic implications. *J. Metamorph. Geol.* 9, 93–109.
- 1200 Mével, C., 2003. Serpentinization of abyssal peridotites at mid-ocean ridges. *Comptes Rendus*
1201 *Geosci.* 335, 825–852.
- 1202 Michard, A., Goffé, B., Avigad, D., 2004. The high-pressure metamorphic front of the south
1203 Western Alps (Ubaye-Maira transect, France, Italy). *Schweizerische Mineral. und*
1204 *Petrogr. Mitteilungen* 84, 215–235.
- 1205 Miller, J.A., Cartwright, I., 2000. Distinguishing between seafloor alteration and fluid flow
1206 during subduction using stable isotope geochemistry: Examples from Tethyan ophiolites
1207 in the Western Alps. *J. Metamorph. Geol.* 18, 467–482. <https://doi.org/10.1046/j.1525-1314.2000.00274.x>
- 1208
- 1209 Molina, J.F., Poli, S., 2000. Carbonate stability and fluid composition in subducted oceanic
1210 crust: An experimental study on H₂O-CO₂-bearing basalts. *Earth Planet. Sci. Lett.* 176,
1211 295–310. [https://doi.org/10.1016/S0012-821X\(00\)00021-2](https://doi.org/10.1016/S0012-821X(00)00021-2)
- 1212 O’Hanley, D.S., 1996. *Serpentinites*. Oxford University Press on Demand.
- 1213 O’Neil, J.R., Clayton, R.N., Mayeda, T.K., 1969. Oxygen isotope fractionation in divalent
1214 metal carbonates. *J. Chem. Phys.* 51, 5547–5558. <https://doi.org/10.1063/1.1671982>
- 1215 Paul, D., Skrzypek, G., 2007. Assessment of carbonate-phosphoric acid analytical technique
1216 performed using GasBench II in continuous flow isotope ratio mass spectrometry. *Int. J.*
1217 *Mass Spectrom.* <https://doi.org/10.1016/j.ijms.2006.11.006>

- 1218 Peters, D., Pettke, T., 2017. Evaluation of Major to Ultra Trace Element Bulk Rock Chemical
1219 Analysis of Nanoparticulate Pressed Powder Pellets by LA-ICP-MS. *Geostand.*
2
31220 *Geoanalytical Res.* 41, 5–28. <https://doi.org/10.1111/ggr.12125>
4
5
61221 Pettke, T., Oberli, F., Audétat, A., Guillong, M., Simon, A.C., Hanley, J.J., Klemm, L.M.,
7
81222 2012. Recent developments in element concentration and isotope ratio analysis of
9
10
111223 individual fluid inclusions by laser ablation single and multiple collector ICP-MS. *Ore*
12
131224 *Geol. Rev.* <https://doi.org/10.1016/j.oregeorev.2011.11.001>
14
15
161225 Piccoli, F., Vitale, A., Beyssac, O., Martinez, I., Ague, J.J., Chaduteau, C., 2016. Carbonation
17
181226 by fluid – rock interactions at high-pressure conditions : Implications for carbon cycling
19
20
211227 in subduction zones. *Earth Planet. Sci. Lett.* 1, 1–14.
22
231228 <https://doi.org/10.1016/j.epsl.2016.03.045>
24
25
261229 Poli, S., 2015. Carbon mobilized at shallow depths in subduction zones by carbonatitic liquids.
27
281230 *Nat. Geosci.* 8, 633–636. <https://doi.org/10.1038/ngeo2464>
29
30
311231 Poli, S., Franzolin, E., Fumagalli, P., Crottini, A., 2009. The transport of carbon and hydrogen
32
331232 in subducted oceanic crust: An experimental study to 5 GPa. *Earth Planet. Sci. Lett.* 278,
34
351233 350–360. <https://doi.org/10.1016/j.epsl.2008.12.022>
36
37
381234 Rampone, E., Hofmann, A.W., Piccardo, G.B., Vannucci, R., Bottazzi, P., Ottolini, L.,
39
401235 Hofmann, W., Piccardo, B., Vannucci, R., Bottazzi, P., Ottolini, L., 1996. Trace element
41
421236 and isotope geochemistry of depleted peridotites from an N-MORB type ophiolite
43
44
451237 (Internal Liguride, N. Italy). *Contrib. to Mineral. Petrol.* 123, 61–76.
46
471238 <https://doi.org/10.1007/s004100050143>
48
49
501239 Rampone, E., Piccardo, G.B., Hofmann, A.W., 2008. Multi-stage melt-rock interaction in the
51
521240 Mt. Maggiore (Corsica, France) ophiolitic peridotites: Microstructural and geochemical
53
54
551241 evidence. *Contrib. to Mineral. Petrol.* 156, 453–475. <https://doi.org/10.1007/s00410-008->
56
571242 0296-y
58
59
601243 Sapienza, G.T., Scambelluri, M., Braga, R., 2009. Dolomite-bearing orogenic garnet
61
62
63
64
65

- 1244 peridotites witness fluid-mediated carbon recycling in a mantle wedge (Ulten Zone,
1245 Eastern Alps, Italy). *Contrib. to Mineral. Petrol.* 158, 401–420.
2
31246 <https://doi.org/10.1007/s00410-009-0389-2>
4
5
61247 Scambelluri, M., Bebout, G.E., Belmonte, D., Gilio, M., Campomenosi, N., Collins, N.,
7
81248 Crispini, L., 2016. Carbonation of subduction-zone serpentinite (high-pressure
9
10
111249 ophicarbonates ; Ligurian Western Alps) and implications for the deep carbon cycling.
12
131250 *Earth Planet. Sci. Lett.* 441, 155–166. <https://doi.org/10.1016/j.epsl.2016.02.034>
14
15
161251 Scambelluri, M., Hoogerduijn Strating, E.H., Piccardo, G.B., Vissers, R.L.M., Rampone, E.,
17
181252 1991. Alpine olivine- and titanian clinohumite-bearing assemblages in the Erro-Tobbio
19
201253 peridotite (Voltri Massif, NW Italy). *J. Metamorph. Geol.* 9, 79–91.
21
22
231254 Scambelluri, M., Muntener, O., Hermann, J., Piccardo, G.B., Trommsdorff, V., 1995.
24
251255 Subduction of water into the mantle: history of an Alpine peridotite. *Geology*.
26
27
281256 [https://doi.org/10.1130/0091-7613\(1995\)023<0459:SOWITM>2.3.CO;2](https://doi.org/10.1130/0091-7613(1995)023<0459:SOWITM>2.3.CO;2)
29
301257 Scambelluri, M., Tonarini, S., 2012. Boron isotope evidence for shallow fluid transfer across
31
32
331258 subduction zones by serpentinitized mantle. *Geology* 40, 907–910.
34
351259 Schwartz, S., Guillot, S., Reynard, B., Lafay, R., Debret, B., Nicollet, C., Lanari, P., Auzende,
36
37
381260 A.L., 2013. Pressure temperature estimates of the lizardite/antigorite transition in high
39
401261 pressure serpentinites. *Lithos* 178, 197–210.
41
42
431262 Schwarzenbach, E.M., Früh-Green, G.L., Bernasconi, S.M., Alt, J.C., Plas, A., 2013.
44
451263 Serpentinization and carbon sequestration: A study of two ancient peridotite-hosted
46
471264 hydrothermal systems. *Chem. Geol.* 351, 115–133.
48
49
501265 <https://doi.org/10.1016/j.chemgeo.2013.05.016>
51
521266 Sharma, S. Das, Patil, D.J., Gopalan, K., 2002. Temperature dependence of oxygen isotope
53
54
551267 fractionation of CO₂ from magnesite-phosphoric acid reaction. *Geochim. Cosmochim.*
56
571268 *Acta.* [https://doi.org/10.1016/S0016-7037\(01\)00833-X](https://doi.org/10.1016/S0016-7037(01)00833-X)
58
59
601269 Spandler, C., Pettke, T., Rubatto, D., 2011. Internal and External Fluid Sources for Eclogite-
61
62
63
64
65

- 1270 facies Veins in the Monviso Meta-ophiolite, Western Alps: Implications for Fluid Flow
1271 in Subduction Zones. *J. Petrol.* 52, 1207–1236. [https://doi.org/10.1093/](https://doi.org/10.1093/petrology/egr025)
2 [petrology/egr025](https://doi.org/10.1093/petrology/egr025)
- 3 1272 Stöckhert, B., 2002. Stress and deformation in subduction zones: insight from the record of
4
5
6 1273 exhumed metamorphic rocks. *Geol. Soc. London, Spec. Publ.*
7
8 1274 <https://doi.org/10.1144/gsl.sp.2001.200.01.15>
9
- 10
11 1275 Tartarotti, P., Guerini, S., Rotondo, F., Festa, A., Balestro, G., Bebout, G.E., Cannà, E.,
12
13 1276 Epstein, G.S., Scambelluri, M., 2019. Superposed Sedimentary and Tectonic Block-In-
14
15 1277 Matrix Fabrics in a Subducted Serpentinite Mélange (High-Pressure Zermatt Saas
16
17
18 1278 Ophiolite , Western Alps). *Geosciences* 9, 1–29.
19
20 1279 <https://doi.org/10.3390/geosciences9080358>
21
22
- 23 1280 Treves, B., Hickmott, D., Vaggelli, G., 1995. Texture and microchemical data of oceanic
24
25 1281 hydrothermal calcite veins, northern Apennine ophiolites. *Ofioliti* 20, 111–122.
26
- 27
28 1282 Treves, B.E., Harper, G.D., 1994. Exposure of serpentinites on the ocean floor: sequence of
29
30 1283 faulting and hydrofracturing in the northern Apennine ophiolites. *Ofioliti*.
31
- 32
33 1284 Tricart, P., Lemoine, M., 1991. The Queyras ophiolite West of Monte Viso (Western Alps):
34
35 1285 Indicator of a peculiar ocean floor in the mesozoic tethys. *J. Geodyn.*
36
37 1286 [https://doi.org/10.1016/0264-3707\(91\)90037-F](https://doi.org/10.1016/0264-3707(91)90037-F)
38
39
- 40 1287 Vissers, R.L.M., Drury, M.R., Hoogerduijn^Strating, E.H., Spiers, C.J., van der Wal, D., 1995.
41
42 1288 Mantle shear zones and their effect on lithosphere strength during continental breakup.
43
44 1289 *Tectonophysics*. [https://doi.org/10.1016/0040-1951\(95\)00033-J](https://doi.org/10.1016/0040-1951(95)00033-J)
45
46
- 47 1290 Vissers, R.L.M., Drury, M.R., Strating, E.H.H., der Wal, D., 1991. Shear zones in the upper
48
49 1291 mantle: A case study in an Alpine Iherzolite massif. *Geology* 19, 990–993.
50
51
- 52 1292 Weissert, H., Bernoulli, D., 1984. Oxygen isotope composition of calcite in Alpine
53
54 1293 ophiocarbonates: a hydrothermal or Alpine metamorphic signal? *Eclogae Geol. Helv.* 77/1,
55
56
57 1294 29–43.
58
- 59 1295 Yamaguchi, A., Ujiie, K., Nakai, S., Kimura, G., 2012. Sources and physicochemical
60
61
62
63
64
65

1296 characteristics of fluids along a subduction-zone megathrust: A geochemical approach
1297 using syn-tectonic mineral veins in the Mugi mélange, Shimanto accretionary complex.
2
3
4 1298 Geochemistry, Geophys. Geosystems 13. <https://doi.org/10.1029/2012GC004137>

5
6 1299

7
8
9
10
11
12
13
14
15
16
17
18
19
20
21
22
23
24
25
26
27
28
29
30
31
32
33
34
35
36
37
38
39
40
41
42
43
44
45
46
47
48
49
50
51
52
53
54
55
56
57
58
59
60
61
62
63
64
65

Figure 1
[Click here to download high resolution image](#)

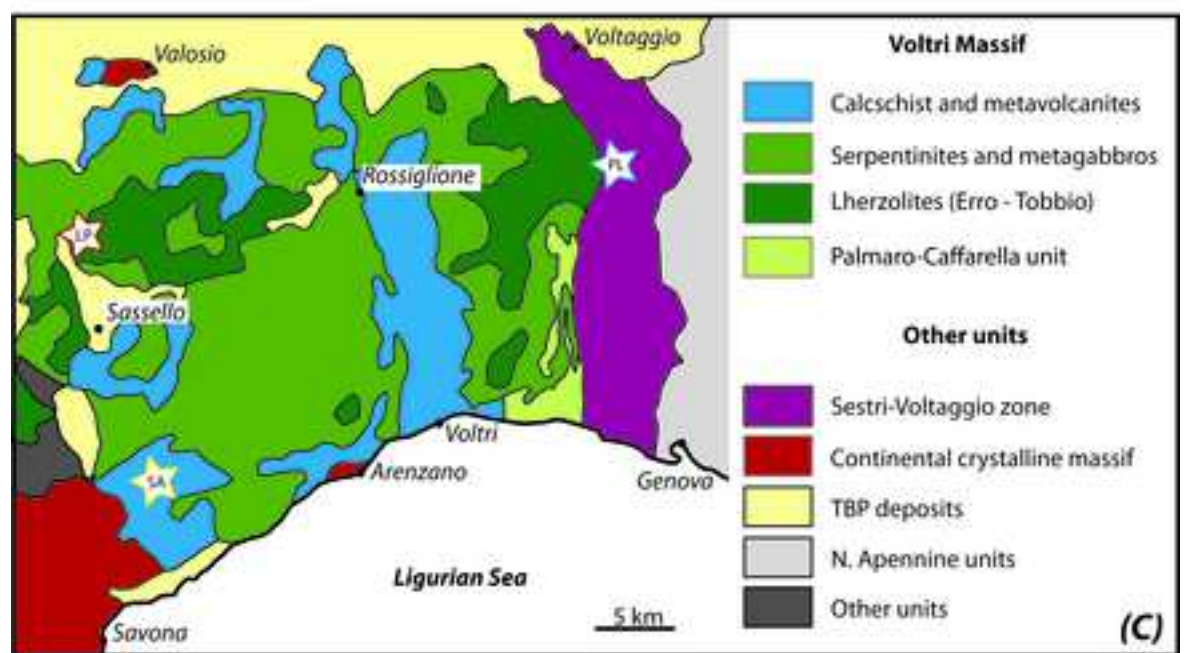
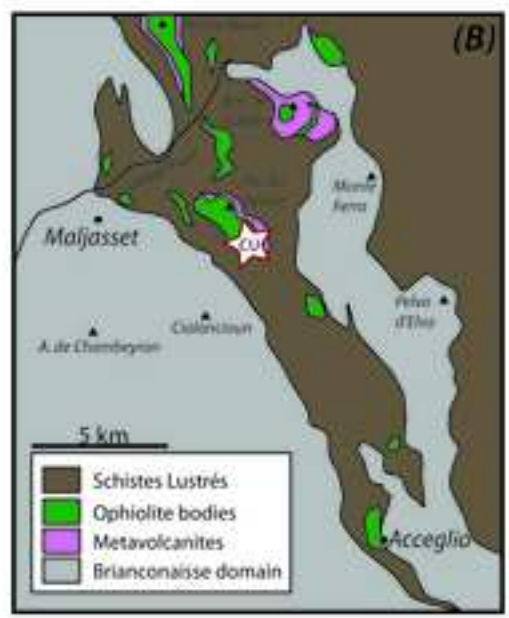
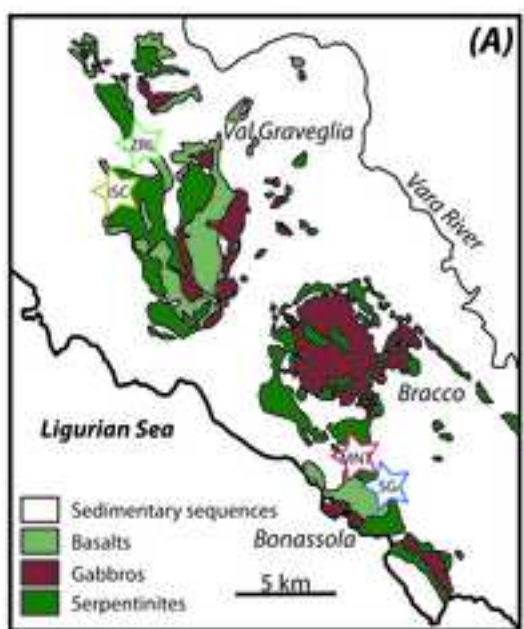
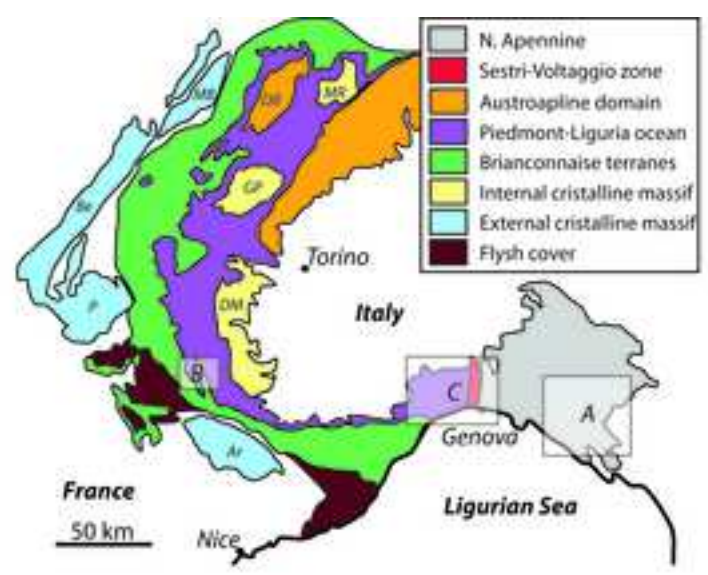


Figure 2
[Click here to download high resolution image](#)

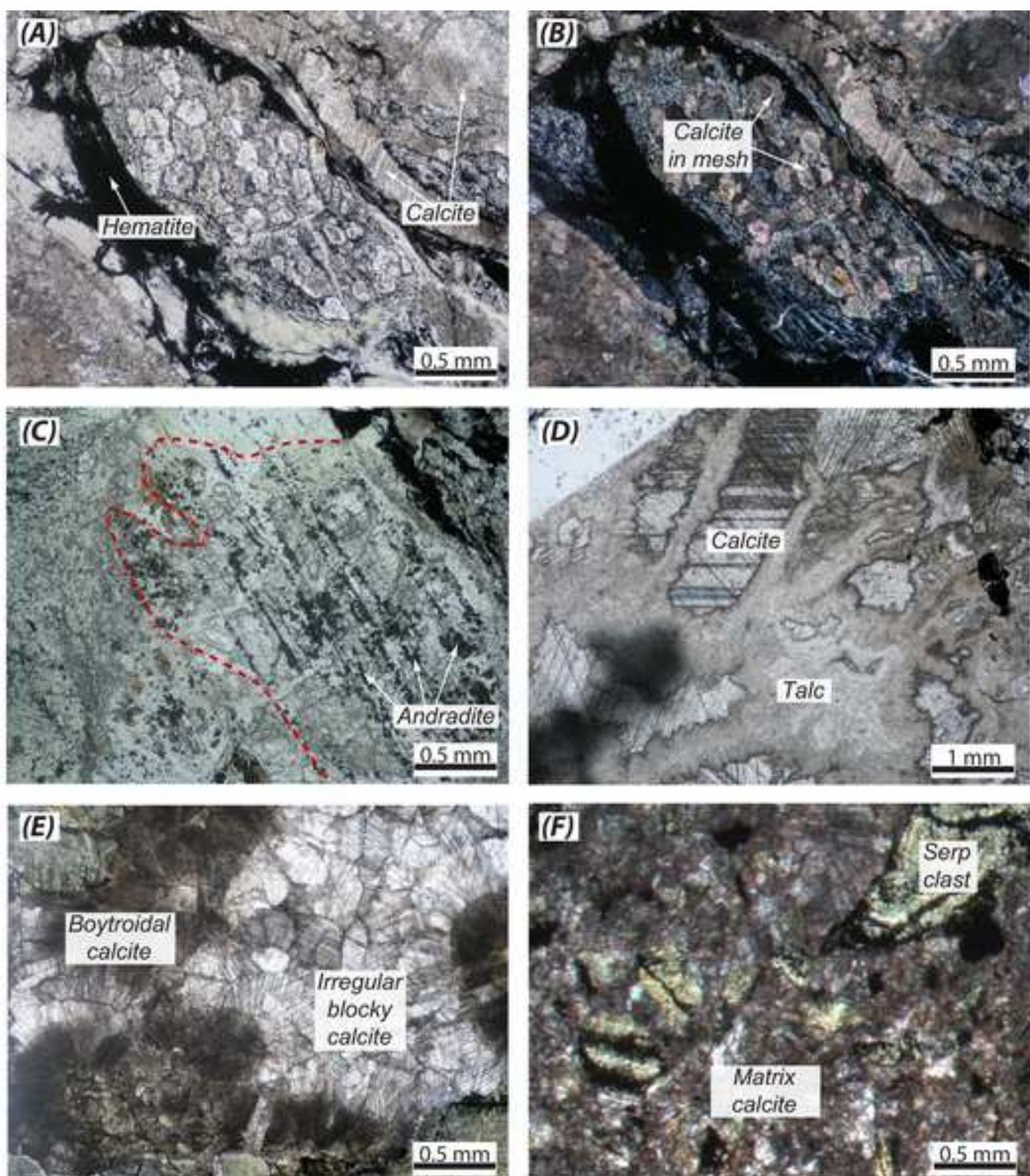


Figure 3
[Click here to download high resolution image](#)

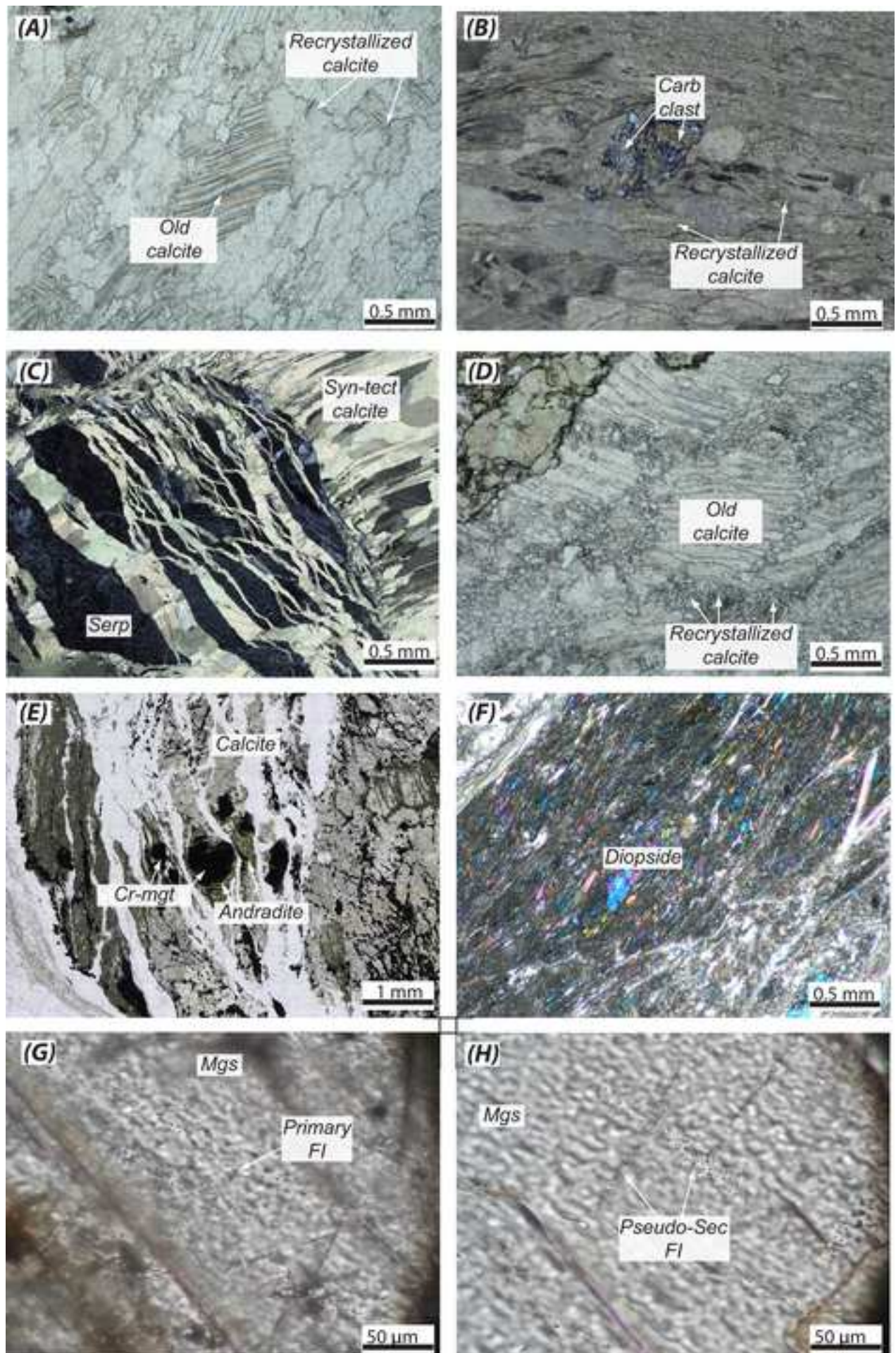


Figure 4

[Click here to download high resolution image](#)

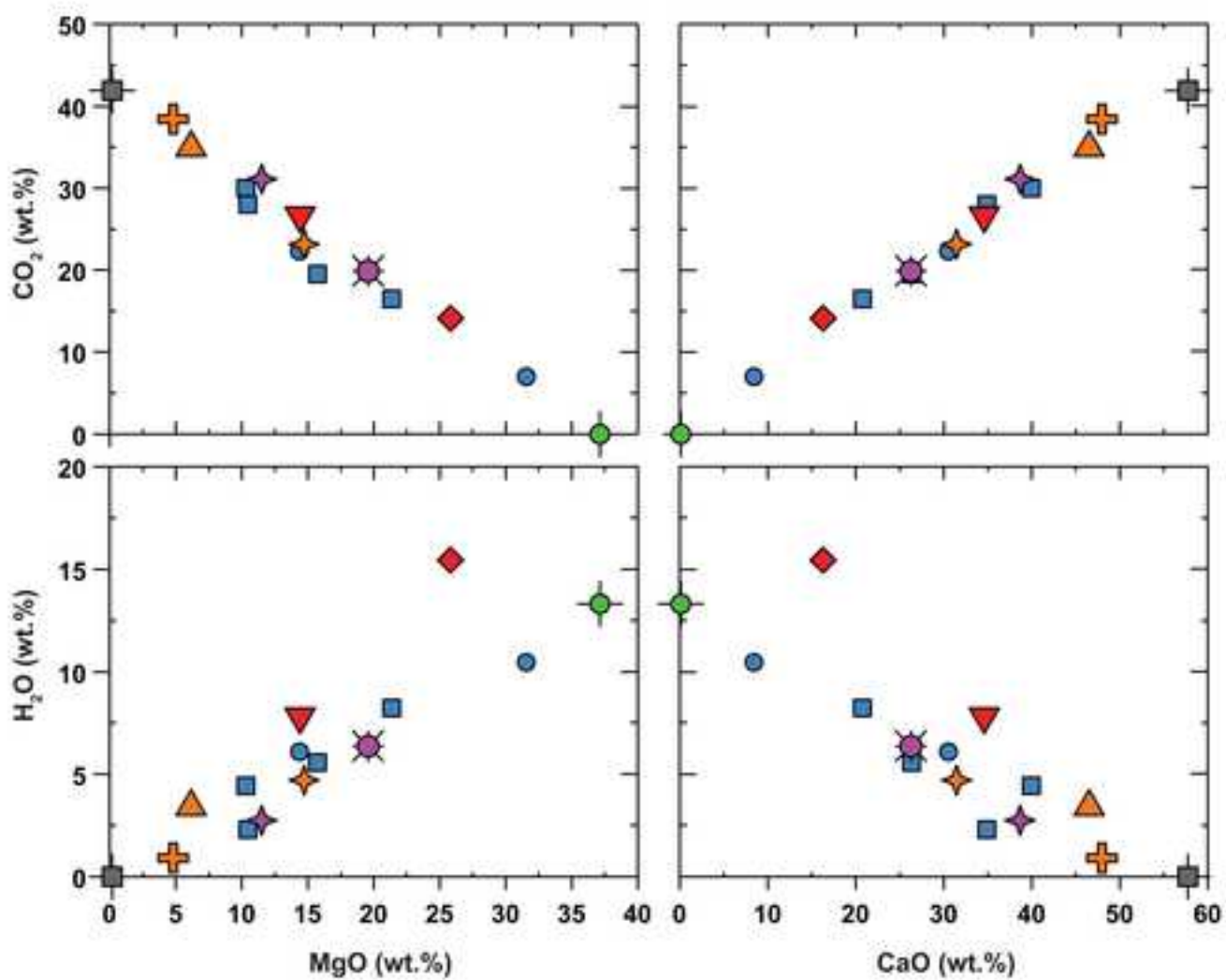
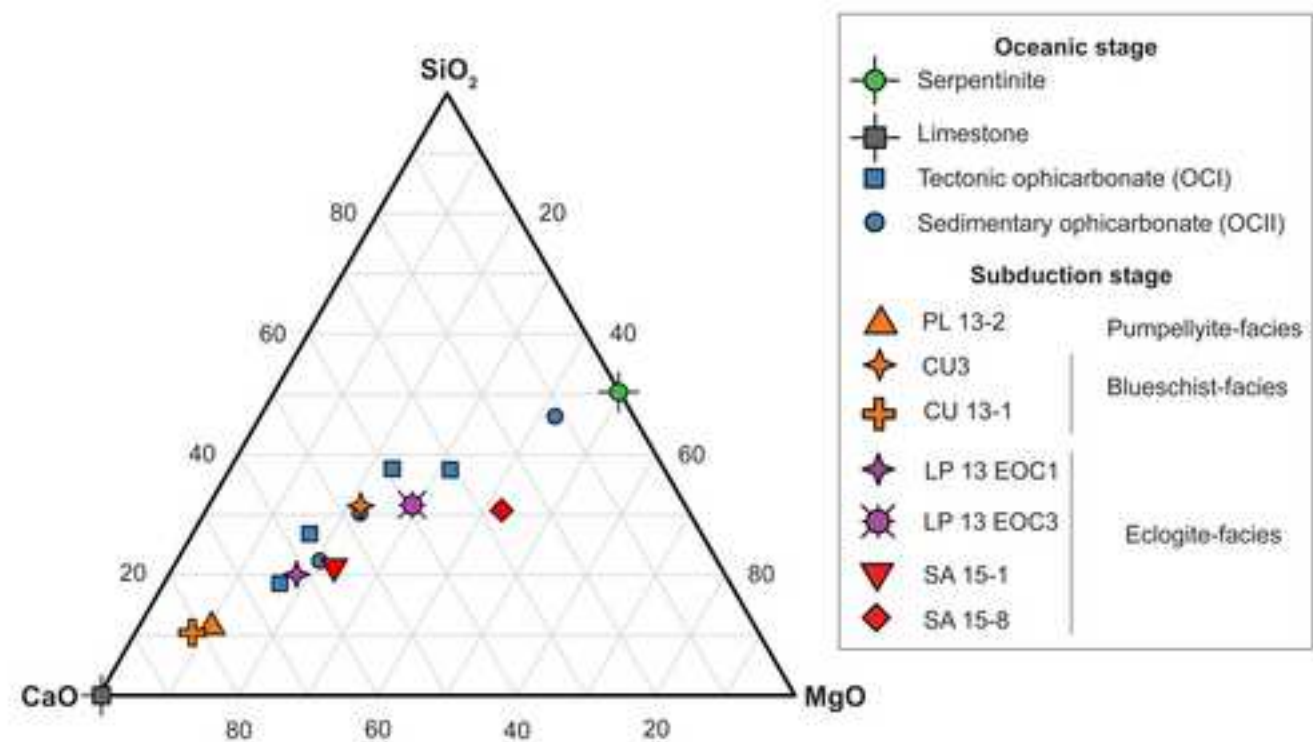


Figure 5
[Click here to download high resolution image](#)

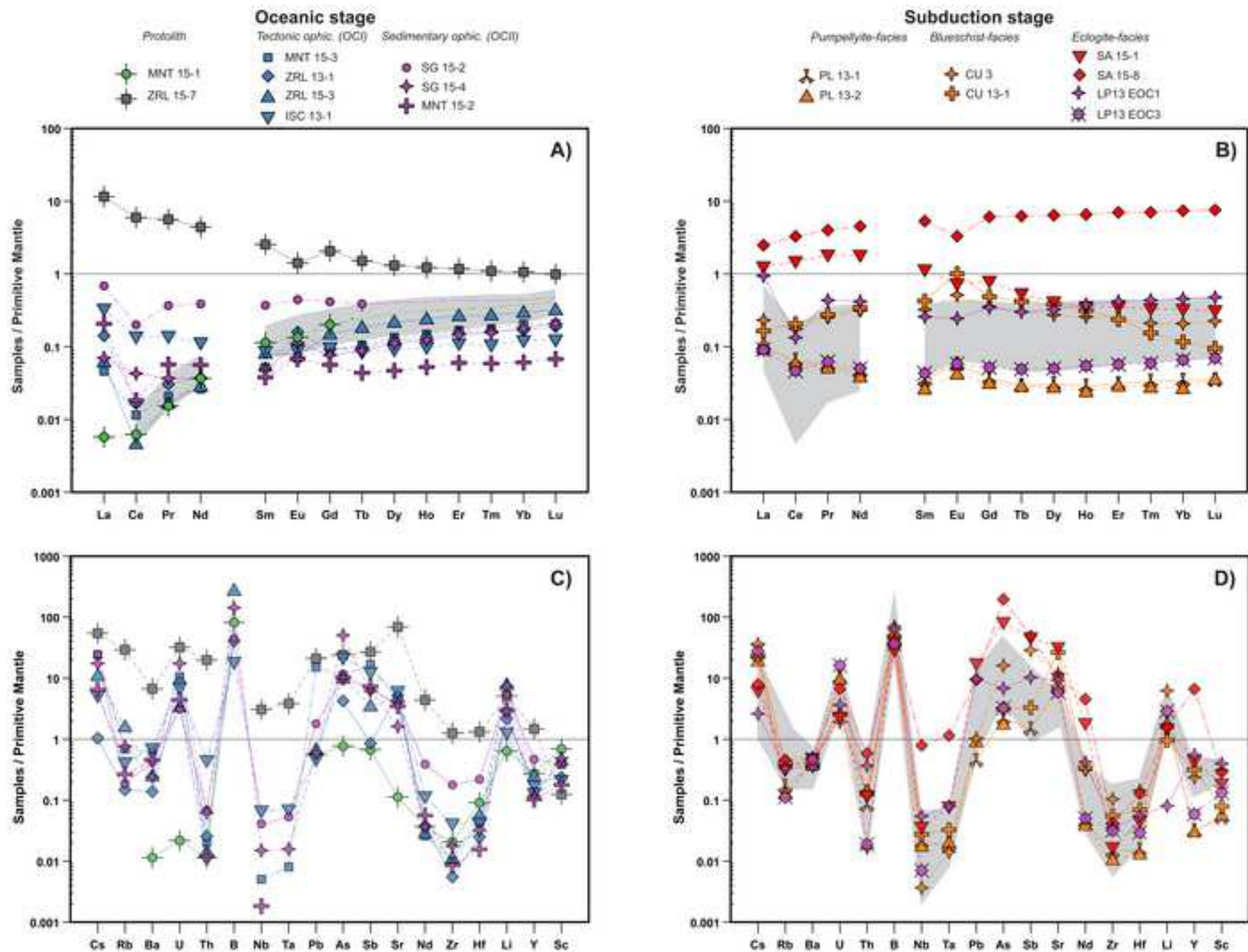


Figure 6
[Click here to download high resolution image](#)

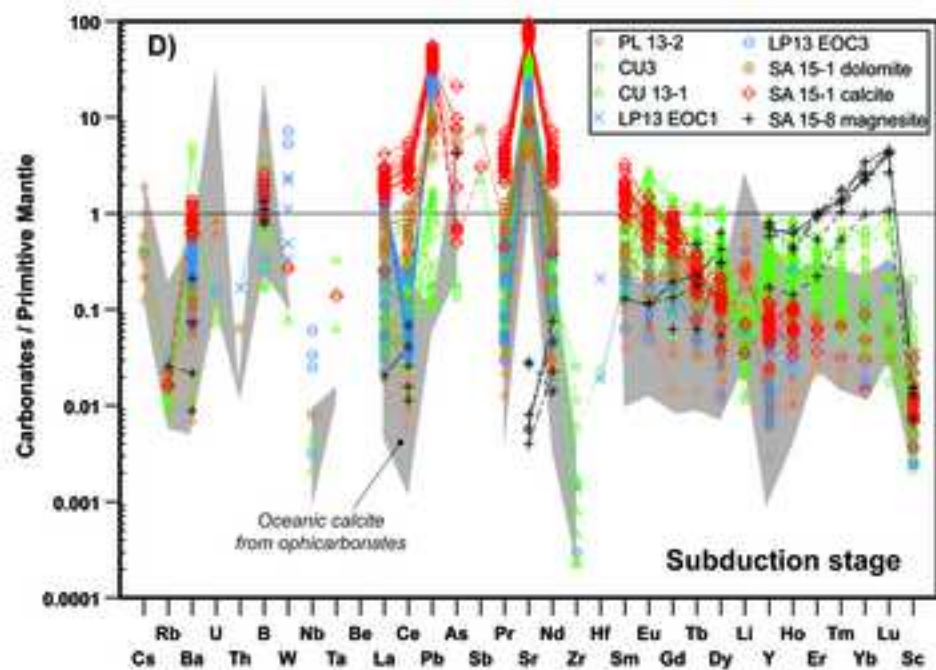
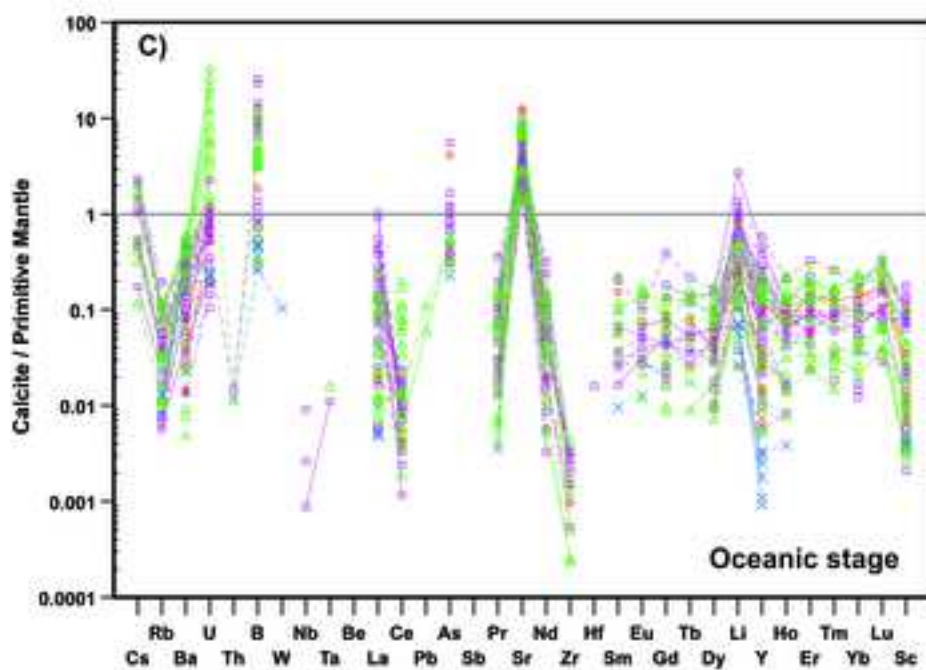
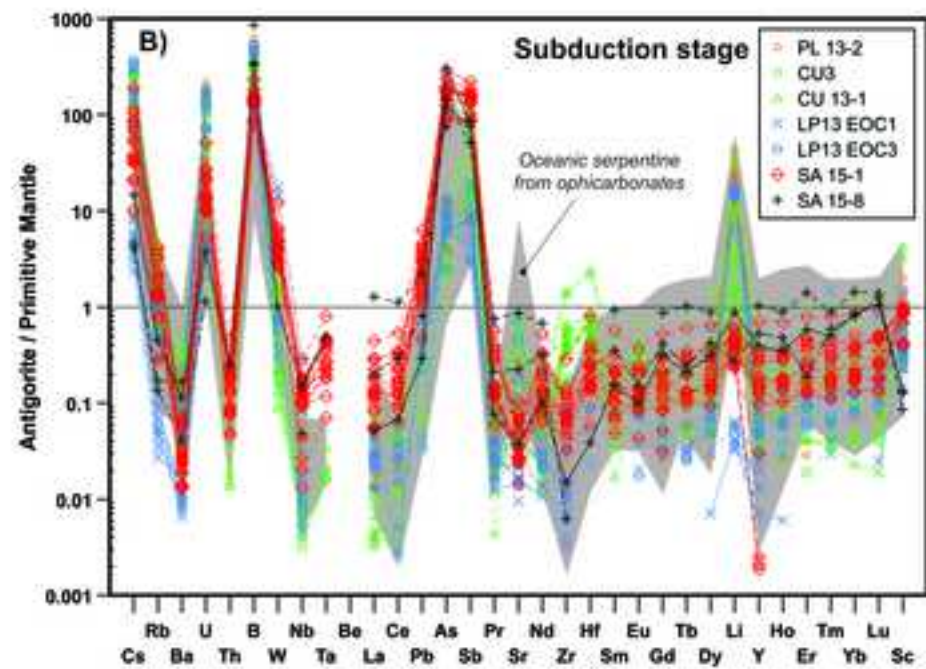
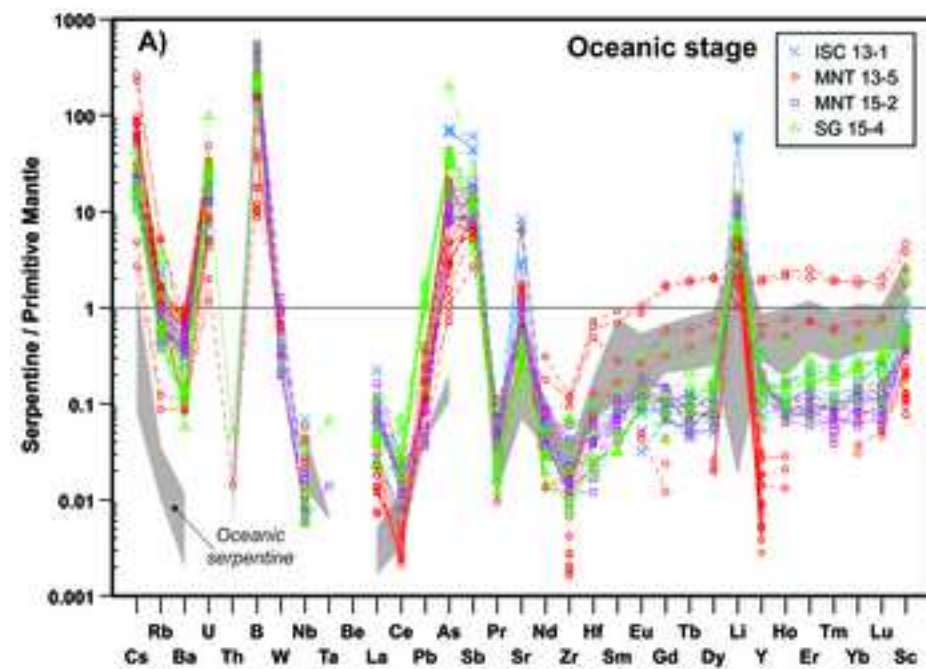


Figure 7
[Click here to download high resolution image](#)

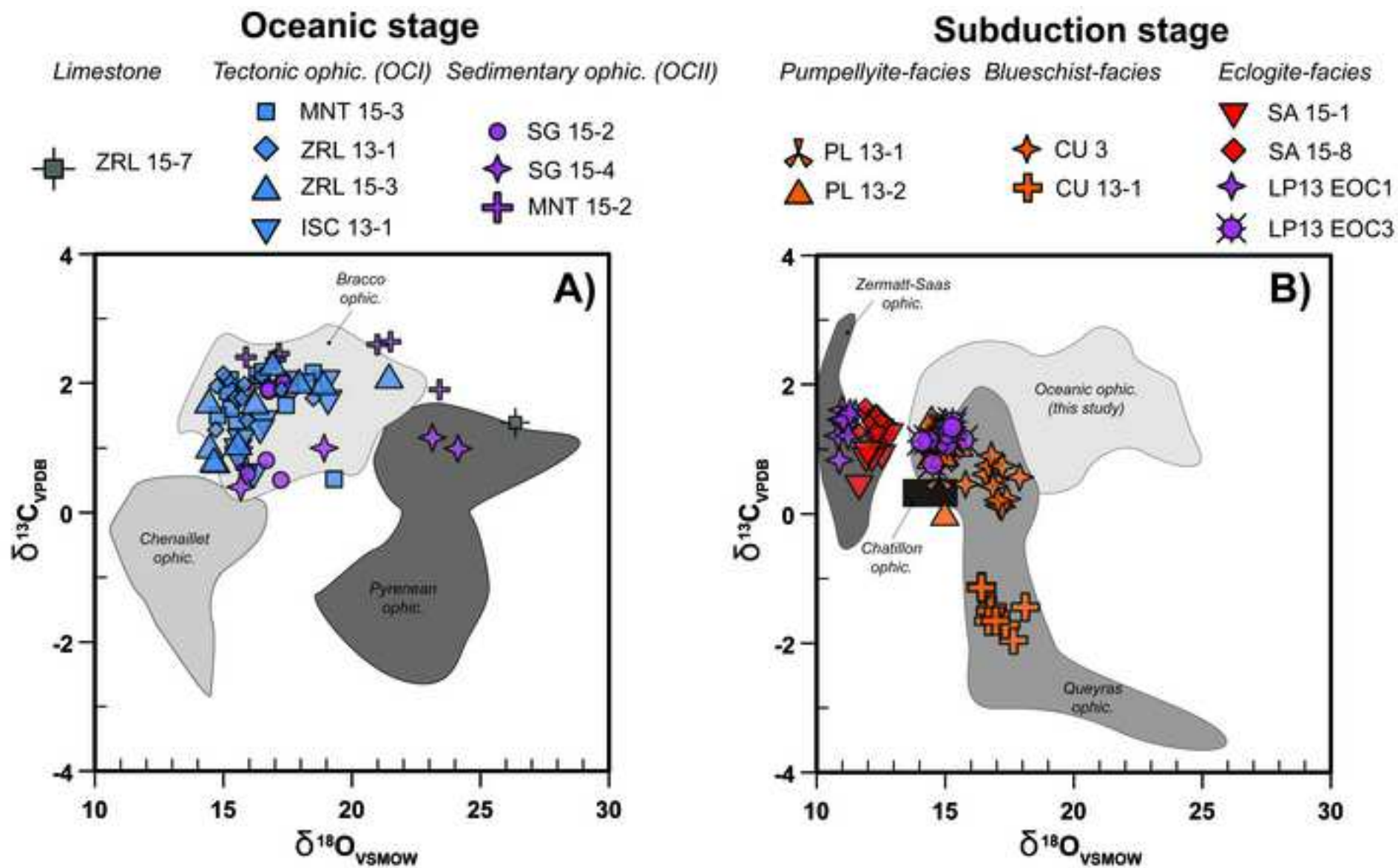


Figure 8

[Click here to download high resolution image](#)

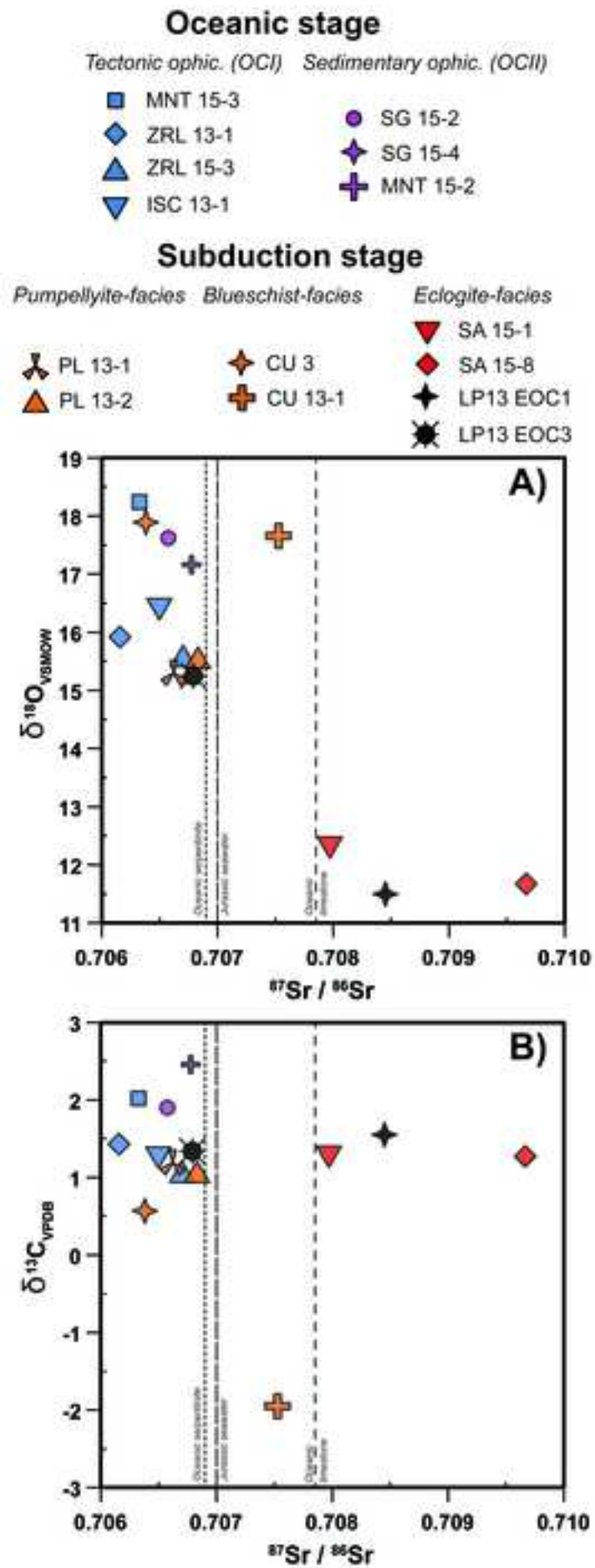


Figure 9
[Click here to download high resolution image](#)

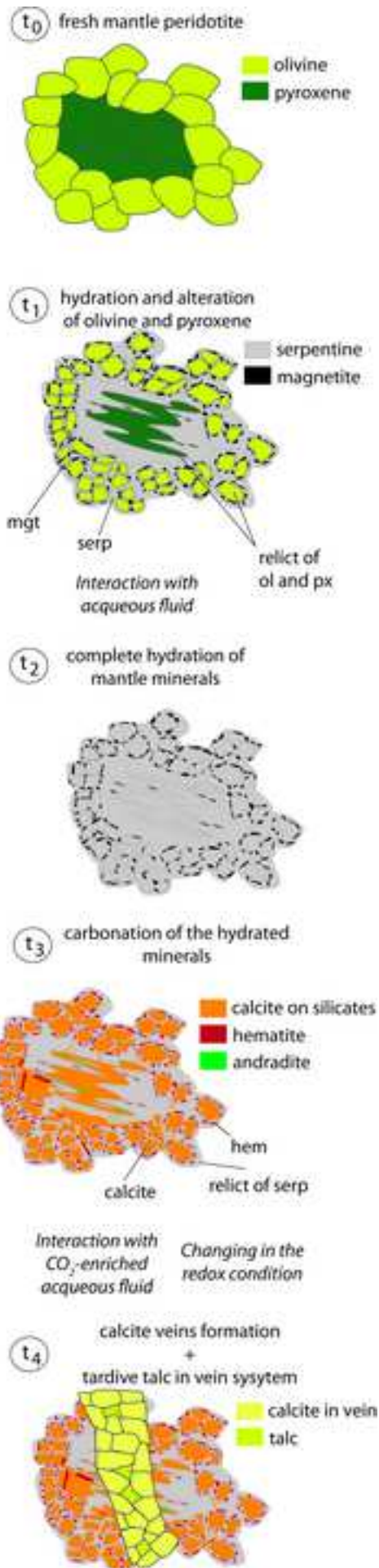


Figure 10

[Click here to download high resolution image](#)

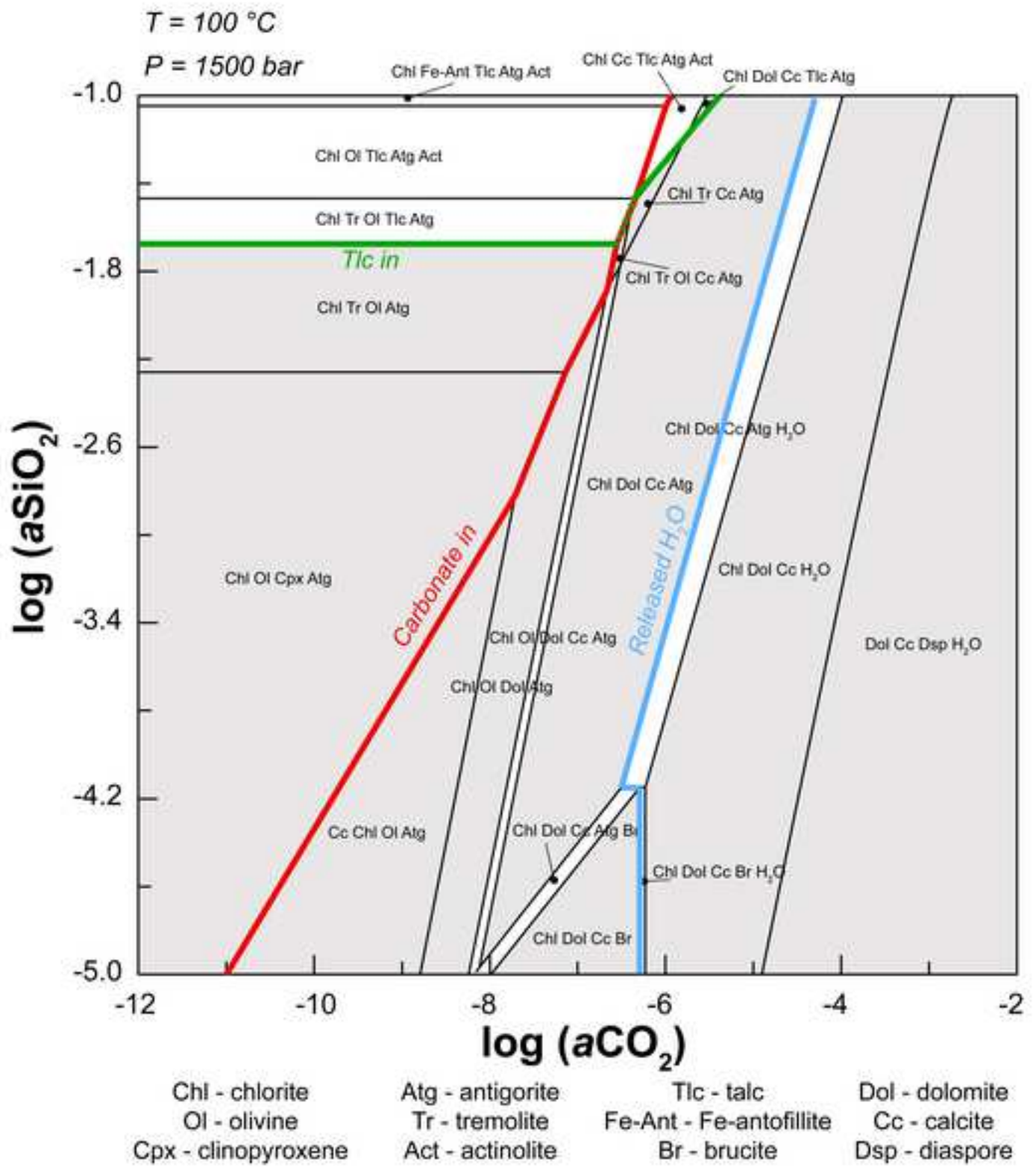


Figure 11
[Click here to download high resolution image](#)

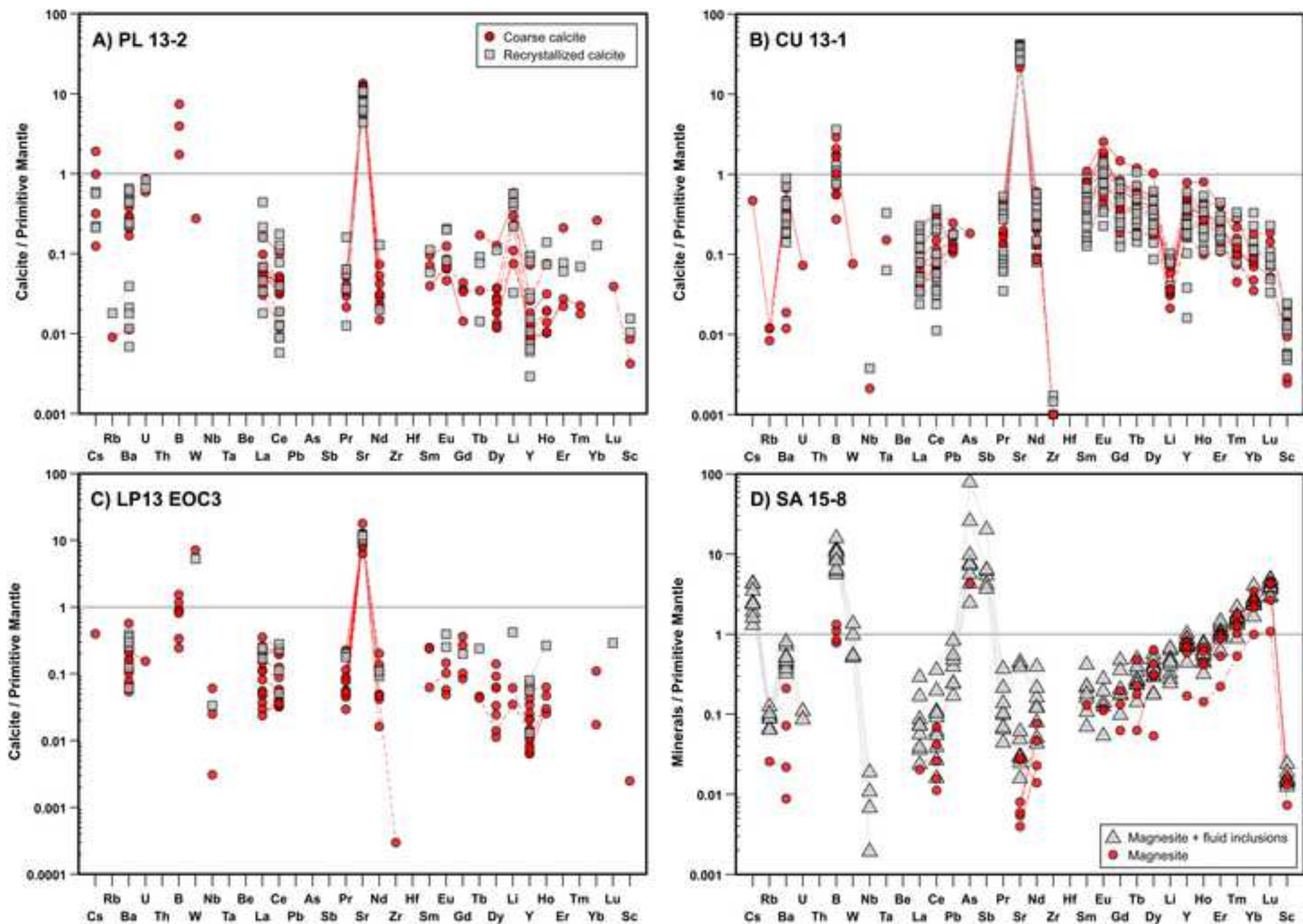


Table 2

[Click here to download Table: Table_2-rev.xlsx](#)**Table 2.** In situ major (in wt.%) and trace element (in ppm) composition of serpentine minerals

	MNT 15-1						MNT
	<i>after pyroxene (n = 11)</i>		<i>after olivine (n = 8)</i>		<i>mesh (n = 3)</i>		<i>clast (n</i>
	<i>sd</i>	<i>sd</i>	<i>sd</i>	<i>sd</i>	<i>sd</i>	<i>sd</i>	
SiO₂	38.07	0.91	40.35	0.71	35.31	0.92	49.35
TiO₂	0.10	0.05	0.03	0.02	0.03	0.00	0.02
Al₂O₃	3.21	0.92	0.89	0.32	0.59	0.05	1.61
FeO	4.80	1.08	5.04	0.59	12.81	2.16	6.36
MnO	0.14	0.02	0.08	0.01	0.09	0.00	0.12
MgO	41.62	0.77	41.55	0.73	39.14	1.23	26.29
CaO	0.06	0.02	0.06	0.01	0.04	0.00	4.14
Na₂O	<0.01		<0.01		<0.01		0.11
K₂O	<0.01		<0.01		<0.01		0.60
Total	88.00		87.98		88.00		88.12
	<i>n = 10</i>		<i>n = 8</i>		<i>n = 3</i>		<i>n =</i>
Li	2.0	2.4	0.26	0.18	0.061	0.037	9.3
B	50	32	36	11	32	13	43
Sc	32	12	11	5	7.0	0.8	3.6
V	152	79	27	23	16	1	33
Cr	5900	2000	700	600	130	70	1200
Co	13	8	15	4	86	38	132
Ni	380	150	1600	400	2200	600	3100
Zn	12	5	9.2	1.5	8.8	1.0	34
As	0.008	0.002	<0.060		0.007	0.002	0.46
Rb	0.011	0.005	<0.023		0.008	0.001	0.97
Sr	2.5	1.4	2.2	0.5	1.8	0.1	22
Y	2.0	0.8	1.7	1.0	1.4	0.2	0.083
Zr	0.27	0.02	0.25	0.05	0.17	0.03	0.11
Nb	0.020	0.007	<0.017		<0.001		0.013
In	0.018	0.004	<0.014		0.006	0.001	0.012
Sb	<0.004		<0.072		<0.004		0.045
Cs	0.010	0.011	<0.019		0.002	0.000	1.5
Ba	0.032	0.024	<0.126		0.028	0.004	4.2
La	0.002	0.001	<0.013		0.001		0.012
Ce	0.012	0.004	<0.020		0.007	0.000	0.007
Pr	0.006	0.003	<0.011		0.003	0.000	0.005
Nd	0.082	0.028	0.12	0.03	0.052	0.005	0.079
Sm	0.078	0.038	0.21	0.07	0.053	0.012	0.13
Eu	0.036	0.018	<0.028		0.025	0.005	0.051
Gd	0.19	0.07	0.14	0.03	0.12	0.02	0.067
Tb	0.039	0.018	0.030	0.011	0.025	0.003	0.081
Dy	0.33	0.13	0.29	0.10	0.21	0.03	0.29

Table 3

[Click here to download Table: Table_3-rev.xlsx](#)**Table 3.** In situ major (in wt.%) and trace element (in ppm) composition of carbonate minerals from

	MNT 13-5				ISC 13-1			
	<i>clast (n = 14)</i>		<i>vein (n = 5)</i>		<i>clast (n = 28)</i>		<i>vein (n = 4)</i>	
	<i>sd</i>		<i>sd</i>		<i>sd</i>		<i>sd</i>	
SiO₂	<0.01		0.04	0.02	0.21	0.10	0.02	0.01
TiO₂	<0.01		<0.01		0.02	0.02	0.03	0.03
Al₂O₃	<0.01		<0.01		0.01	0.01	0.01	0.01
FeO	<0.01		<0.01		0.17	0.10	0.02	0.01
MnO	0.06	0.04	<0.01		0.20	0.12	0.10	0.09
MgO	0.02	0.01	0.54	0.22	0.51	0.35	0.31	0.18
CaO	54.87	2.54	54.42	0.61	56.02	3.58	56.41	1.74
Na₂O	0.01	0.01	<0.01		0.02	0.01	0.02	0.02
K₂O	<0.01		<0.01		<0.01		<0.01	
Total	54.96		55.00		57.15		56.91	
	<i>n = 14</i>		<i>n = 5</i>		<i>n = 2</i>		<i>n = 7</i>	
Li	0.75	0.47	0.39	0.02	0.094	0.030	0.45	0.09
B	0.48		0.55		0.14	0.05	0.93	0.05
Sc	0.44	0.33	0.30	0.21	0.069	0.008	1.6	0.1
V	0.44	0.34	0.20		0.009	0.005	0.82	0.40
Cr	6.6	2.8	2.7	1.9	1.9	0.2	11	6
Co	1.2	2.1	0.27	0.27	0.21	0.14	4.7	1.8
Ni	36	19	11	6	4.4	2.7	320	150
Zn	0.95	0.45	0.16	0.09	0.26	0.13	7.8	3.0
As	<0.014		0.083	0.108	0.021	0.010	0.092	
Rb	0.023	0.012	<0.007		0.006	0.002	0.024	0.008
Sr	89	26	160	80	120	50	120	10
Y	0.42	0.62	0.25	0.22	0.009	0.004	0.12	0.02
Zr	<0.008		0.010		<0.027		<0.001	
Nb	<0.005		<0.004		<0.003		<0.002	
In	<0.004		<0.003		<0.014		<0.014	
Sb	<0.020		<0.017		<0.075		<0.003	
Cs	<0.004		<0.004		0.026	0.011	0.026	0.011
Ba	0.36	0.18	0.39	0.35	1.5	1.1	1.2	0.3
La	0.014		0.012		0.004	0.002	0.019	
Ce	0.012	0.007	0.007		0.015	0.001	0.015	0.001
Pr	0.011		<0.003		0.001		<0.001	
Nd	0.056		0.025		<0.039		<0.014	
Sm	0.076	0.047	0.062		0.004		<0.018	
Eu	0.026		0.010		0.002		<0.003	
Gd	0.15	0.15	0.040		<0.037		<0.013	
Tb	0.053		0.008		<0.006		<0.001	
Dy	0.13	0.16	0.029	0.004	<0.020		<0.007	
Ho	0.045	0.048	0.013	0.003	0.001		<0.001	
Er	0.16	0.15	0.044	0.019	<0.023		<0.010	
Tm	0.047		0.007	0.001	<0.006		<0.001	

Table 4

[Click here to download Table: Table_4_rev.xlsx](#)

Table 4. Whole-rock C-O and Sr isotopic composition for serpentinite, limestone and ophicarbonates rocks

							<i>Jurassic age</i>		<i>High-pressure age</i>	
		$\delta^{18}\text{O}$ (‰)	$\delta^{13}\text{C}$ (‰)	Rb/Sr	$^{87}\text{Sr}/^{86}\text{Sr}$	err	$^{87}\text{Sr}/^{86}\text{Sr}_{160\text{Ma}}$	Δ (measured-160Ma)	$^{87}\text{Sr}/^{86}\text{Sr}_{33\text{Ma}}$	Δ (measured-33Ma)
<i>Oc. serp.</i>	MNT 15-1	<i>n.d.</i>	<i>n.d.</i>	-	0.706929	0.000038	0.706929	0.000000		
<i>Limestone</i>	ZRL 15-7	26.1	0.5	0.0128	0.707932	0.000009	0.707848	0.000084		
	MNT 13-5	10.9	1.4	0.0048	0.706355	0.000007	0.706323	0.000032		
<i>OCI (tectonic ophic.)</i>	ZRL 13-1	15.7	0.6	0.0009	0.706162	0.000009	0.706156	0.000006		
	ZRL 15-3	15.6	1.1	0.0099	0.706768	0.000016	0.706703	0.000065		
	ISC 13-1	16.2	0.4	0.0020	0.706510	0.000012	0.706497	0.000013		
<i>OClI (sedimentary ophic.)</i>	SG 15-4	17.4	1.1	0.0143	0.705756	0.000009	0.705662	0.000094		
	SG 15-2	15.9	-1.7	0.0015	0.706046	0.000022	0.706036	0.000010		
	MNT 15-2	17.0	1.6	0.0023	0.706790	0.000009	0.706775	0.000015		
	PL 13-1	15.1	0.3	0.0007	0.706624	0.000008	0.706619	0.000005		
<i>Prograde ophicarbonates</i>	PL 13-2	15.3	0.2	0.0005	0.706833	0.000009	0.706830	0.000003		
	CU 3	17.7	-0.3	0.0009	0.706383	0.000008	0.706377	0.000006		
	CU 13-1	17.1	-2.8	0.0005	0.707530	0.000009	0.707527	0.000003		
	SA 15-1_{calcite}	12.5	1.0	<0.0001	0.707969	0.000014	0.707969	0.000000	0.707969	0.000000
<i>Eclogite facies ophicarbonates</i>	SA 15-1_{dolomite}	11.9	0.8	0.0001	0.708130	0.000022	0.708130	0.000000	0.708130	0.000000
	SA 15-8	11.5	0.4	0.0013	0.709670	0.000009	0.709661	0.000009	0.709668	0.000002
	LP13 EOC1	11.3	0.7	0.0011	0.708453	0.000005	0.708446	0.000007	0.708452	0.000001
	LP13 EOC3	15.0	0.5	0.0006	0.706791	0.000010	0.706787	0.000004	0.706790	0.000001

n.d. - not determined

Supplementary Table A1

[Click here to download Background dataset for online publication only: Supplementary-Table-A1.xlsx](#)

Supplementary Table A2

[Click here to download Background dataset for online publication only: Supplementary-Table-A2.xlsx](#)

Supplementary Table A3

[Click here to download Background dataset for online publication only: Supplementary-Table-A3.xls](#)

Appendix Figure A1

[Click here to download Background dataset for online publication only: Appendix_Figure_A1.jpg](#)

Supplementary material S1

[Click here to download Background dataset for online publication only: Supplementary_material_S1.docx](#)